

Quantum Path Computing: A Quantum Computing Architecture
with Feynman's Path Integrals, Wave-Particle Duality and
Entangled Histories*

Burhan Gulbahar

*Department of Electrical and Electronics Engineering,
Ozyegin University, Istanbul 34794, TURKEY*

(Dated: December 14, 2024)

arXiv:1709.00735v2 [quant-ph] 20 Sep 2017

Abstract

Double slit interference experiment is at the heart of quantum mechanics by clearly presenting wave-particle duality and quantum nature for particles as emphasized by Richard Feynman. Previous quantum computing (QC) architectures utilizing wave nature with simple set-ups in combination with quantum superposition interference result in QC speed-up with the cost of exponential increase in resources such as time, space or energy. In this article, wave-particle duality of propagating electrons is exploited in a simple interference set-up to present a novel computing architecture denoted by quantum path computing (QPC) targeting a low complexity QC architecture. It is composed of multiple consecutive planes and Gaussian slits combining path trajectories of the particle nature with constructive and destructive interference measurements of the wave nature. QPC does not explicitly require exponential complexity of resources by utilizing entangled path history inherently existing in set-up with a unique mathematical formulation of Feynman's path integral which naturally includes path histories. It exploits the particle nature with slit positions on each plane by realizing entanglement in tensor product space distributed in the path history of single particle. Hidden subgroup problem (HSP) is solved with QPC in complete analogy with existing period finding algorithms utilizing quantum gate circuits and multiple qubit entanglement resources by creating a fundamental QC tool. QPC promises solutions of particular instances of simultaneous Diophantine approximation problem as a practical and important application while formally determining the computational complexity of the problem solving capability is an open issue. In addition, previous models of interference set-ups analyzing exotic paths in single plane systems are, for the first time, extended to multi-plane set-up while simulations consider non-negligible and important effects of multiple exotic paths compared with previous studies. The challenges are discussed for modeling computational complexity of efficiently solvable problems, designing optimum set-up geometry and experimental aspects including source energy and detection sensitivity depending on problem complexity.

* E-mail: burhan.gulbahar@ozyegin.edu.tr

I. INTRODUCTION

The Young's double slit experiment is one of the fundamental experiments where the foundational laws and the essence of quantum mechanics are contained as emphasized by Richard Feynman with detailed models for electron based system set-up [1]. The importance given to the experiment by Feynman motivates to create a simple design of computing exploiting fundamental laws of quantum mechanics such as *wave-particle duality*. Previous quantum computing (QC) architectures for this target utilizing classical optics as discussed in [2–5] or interferometer structures in [6–16] exploit *wave nature* of quantum mechanical set-ups in combination with the power of quantum superposition. They achieve QC speed-up with the cost of exponential complexity of resources such as in time, space or energy domains. The fact that utilizing quantum superposition based on wave properties is not sufficient alone supports an intuitive approach to include *particle nature* of electrons in addition to wave properties while promising entanglement resources. In this article, a novel computing solution denoted by quantum path computing (QPC) achieves to realize tensor product subspaces and to perform computing by combining two special features: consecutive planes with *entangled histories of particle trajectory through slits as multiple qudit representations* (multi-dimensional quantum state) and *parallel computation of a special black box function* based on the unique formulation using Feynman's path integrals inherently including entangled path histories and Gaussian slits simplifying integral outputs [1]. QPC set-up is completely different from a simple isomorphism between exponentially large states of a single particle [3, 17, 18]. It achieves to realize S_T^{N-1} states of $N-1$ qudits (corresponding to $N-1$ consecutive planes) with S_T quantum states for each qudit (corresponding to S_T slits in each plane) by utilizing polynomial complexity of spatial resources. Entanglement obtained with path histories on the planes is compatible with conceptual framework in recent works discussing specific examples of entangled quantum trajectories where it is emphasized that histories are explicit elements of Feynman's path integral [19–22]. Therefore, QPC brings a novel tool to realize QC architectures with single particles while exploiting entanglement in time domain rather than relying on spatially separated multiple qubit representations.

QC systems are recently promising quantum supremacy with various architectures such as superconducting structures, quantum dots or trapped ions [23], annealing based adiabatic architectures [24], topological quantum computing [25] and boson sampling methods

[26, 27]. Fundamental problems in quantum circuit based systems are noise with imperfections in quantum operations and decoherence due to entanglement of qubits with outside environments [28]. Operation temperature, complexity of hardware and small number of qubit realizations are other fundamental challenges. QPC is a simple system design and mathematical model compatible with naturally inspired architectures with adaptability to different interference mediums of particle trajectories including photons while promising room temperature operation [29]. QPC utilizes both superposition of the wave nature and entanglement property of the particle nature within a tensor product space of histories to calculate a functional output for all qudit states in polynomial time complexity. Therefore, wave-particle duality as clearly emphasized by Feynman for double-slit experiment is, for the first time, exploited in a simple QC design without explicitly requiring exponential complexity of resources while the fundamental open issues are discussed in Section IX.

QPC is different compared with architectures utilizing classical optics [2–5] or various interferometer set-ups [6–16] requiring exponentially large resources and utilized for factoring problems, implementation of Gauss sum, generalized truncated Fourier sums and similar problems. On the other hand, in [6], a similar conceptual set-up is utilized for polynomial solution of traveling salesman problem. However, proposed model requires solution for a specific path without concentrating on particle property. It requires exponentially large energy or number of particles to achieve polynomial solution. More attempts utilizing delay based optical systems [7–9], fiber optical set-ups [10] and nano-optical setups [11] for solutions of NP-complete problems are presented while problems regarding exponential delays, energy consumptions or space are emphasized. Interference based solutions are not based on path integrals, not utilizing wave-particle duality and not providing a direct one-to-one analogy with period finding QC algorithms. QPC proposes a mathematical framework utilizing overall superposition intensity with constructive and destructive interferences rather than individual paths and combines entanglement in path histories as a computing tool.

Boson sampling methods are future promising as candidates for realizing a simplified implementation of QC with various modes of single photon, passive linear optics such as beamsplitters and phase-shifters, and photodetection while having challenges for experimental implementation [26, 30]. Passive linear optics has the potential for outperforming classical computers due to the hardness of solving boson sampling problem classically, e.g., calculating matrix permanents, while still having challenges to solve practical mathematical

problems. QPC has similarity in terms of simplicity, sampling from the probability distribution and collecting multiple particles on screen compared with boson sampling while requiring simpler hardware, i.e., slit planes, detector screen (promising a simpler design compared with single photon modes in boson sampling), Gaussian slits and sources, and the medium for free space propagation, while targeting a practical number theoretic problem, i.e., simultaneous Diophantine approximation (SDA) problem and non-uniform lattices.

Double slit experiments are recently getting more attention to analyze exotic paths of particles, Gouy phase effect in measurement of Sorkin parameter and fundamentals of Born rule [31–34]. Simplicity of slit based interference experiments and experimental verification in recent studies further support feasibility of QPC design. QPC extends, for the first time, previous formulation to multi-plane set-ups while simulating effects of multiple exotic paths compared with previous studies utilizing single path analysis [31–33].

In this article, QPC set-up is utilized to create a computing solution of period finding type for hidden subgroup problems (HSPs). The analogy with period finding QC algorithms utilizing quantum gates and multiple-qubit entanglement resources is explicitly provided promising QPC as a fundamental tool to be utilized in future architectures. QPC promises a framework for polynomial time solutions of *particular instances* of SDA problems which are known to be NP-hard to find the best approximation [35] or problems related to generating reciprocal lattices of non-uniform lattices. Formal determination of the complexity class of problems to be efficiently solved is an open future issue. Numerical simulations are performed by also accurately considering effects of exotic paths discussed in [31–34] and observing their significant effects which cannot be neglected in QPC based set-ups. Open issues and challenges for realizing QPC prototype such as problem modeling which are efficiently solvable, optimum geometrical design of slits and planes, and experimental aspects including source energy, sensor sensitivity and slit design are discussed in Section IX.

The remainder of the paper is organized as follows. In Section II, physical set-up of QPC is presented. In Sections III and IV, entanglement resources with path histories and fundamental model of QPC based on Feynman’s path integral formalism are presented, respectively. Then, in Section V, fundamental formulation of QC power is modeled while in Section VI, solutions for HSPs and SDA problems are presented. In Section VII, effects of exotic paths are modeled while in Section VIII, numerical simulations are performed. Finally, in Sections IX and X, open issues and conclusions are presented, respectively.

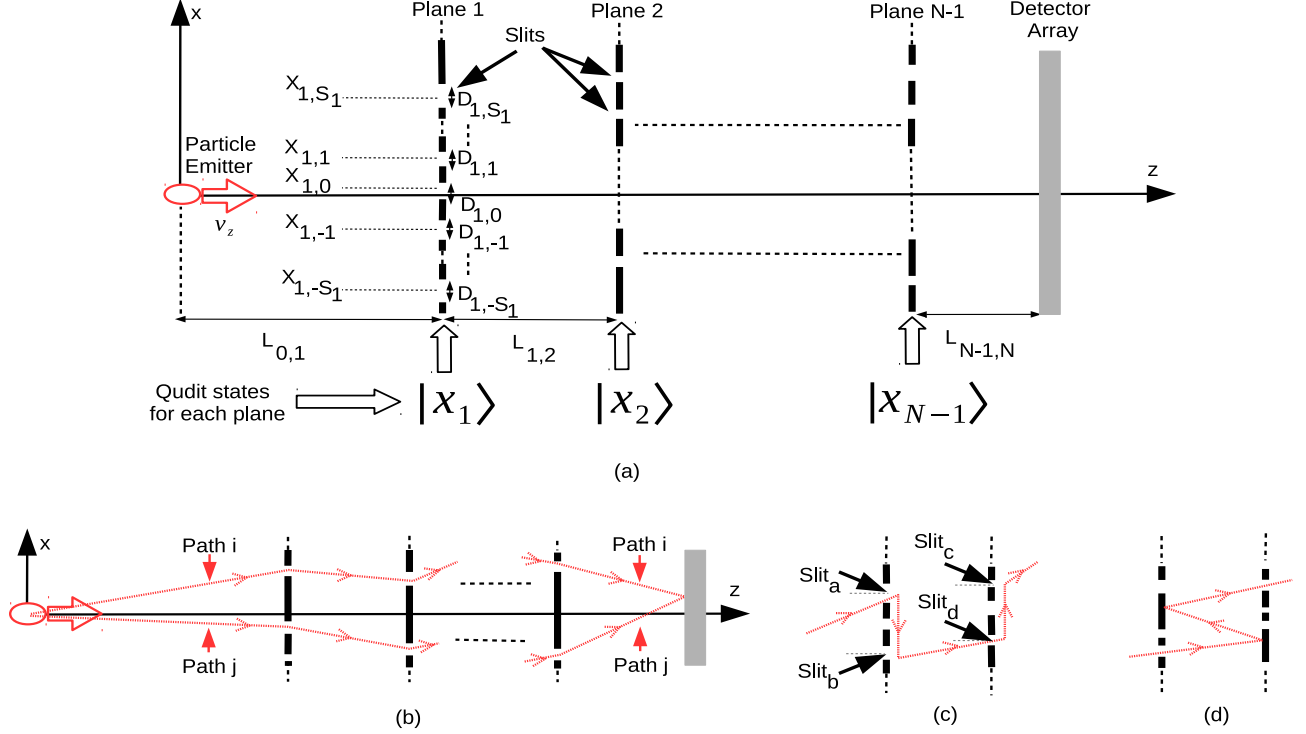


FIG. 1. (a) Quantum path computing (QPC) architecture with multiple, consecutive and parallel planes of slits, and qudit representations for entangled path histories, (b) i th and j th paths interfering on the detector array or image plane, and (c) exotic path among the slits with indices a , b , c and d , and (d) reflecting paths between consecutive planes of slits.

II. SYSTEM ARCHITECTURE

Assume that there are $N - 1$ planes of slits in front of a particle source such as electrons or neutrons, and interference pattern behind the last plane, i.e., plane with the index $N - 1$, is observed by a detector array (image or sensor plane) denoted by the plane index N as shown in Fig. 1(a). Particles are assumed to perform free space propagation. The j th plane has $S_{j,T} \equiv 2S_j + 1$ number of slits where the central positions and widths of slits are given by $X_{j,i}$ and $D_{j,i}$, respectively, where $j \in [1, N - 1]$ and $i \in [-S_j, S_j]$, and the set of ordered slit positions on j th plane is denoted by column vector \vec{X}_j . Row vectors are represented with the transpose operation, i.e., $(\cdot)^T$. In the following sections, widths of the slits are chosen uniformly along each plane but differently among planes. The whole set of slit positions on $N - 1$ parallel planes are denoted by \mathbf{X}_{N-1} . Distance between i th and j th planes is given by $L_{i,j}$ where the distances from particle emission source to the first plane and from $(N - 1)$ th

plane to the detection plane are given by $L_{0,1}$ and $L_{N-1,N}$, respectively. Behavior of particle is assumed to be classical in z -axis with the velocity given by v_z while quantum superposition interference is assumed to be observed in x -axis as a one dimensional model. The model can be easily extended to two dimensional (2D) systems. Distance between planes is assumed to be much larger compared with widths and positions of slits in x -axis.

Time duration for the particle to travel between $(j-1)$ th and j th planes is assumed to be $t_{j-1,j} = v_z / L_{j-1,j}$ for $j \in [1, N]$ where $t_{N-1,N}$ denotes the observation time after the particle passes through $(N-1)$ th plane. Position in x -axis on j th plane is denoted by x_j while the wave functions of a specific n th path and superposition of all previous paths on j th plane are denoted by $\Psi_{n,j}(x_j)$ and $\Psi_j(x_j)$, respectively. Inter-plane distance and inter-plane duration vectors are represented by $\vec{L} = [L_{0,1} \dots L_{N-1,N}]$ and $\vec{t} = [t_{0,1} \dots t_{N-1,N}]$, respectively. Paths of the particle are assumed to be indexed by n for $n \in [0, N_p - 1]$ as shown in Fig. 1(b) where $N_p = \prod_{j=1}^{N-1} S_{j,T}$ and $Path_n \equiv \{s_{n,1}, s_{n,2}, \dots s_{n,N-1}; s_{n,j} \in [-S_j, S_j]\}$. Therefore, slit position for n th path on j th plane is given by $X_{n,s_{n,j}}$. The number of paths given by N_p can be significantly large for even a small number of planes and slits, e.g., reaching $> 10^{12}$ distinct paths interfering on detector plane for $N-1 = 12$ and $S_j = 5$ for $j \in [1, 12]$. There are some assumptions making the model more clarified:

- Plane material is assumed to be absorbing without particle reflection between slits making calculation much more complicated as shown in Fig. 1(d) while exotic paths are taken into account as shown in Fig. 1(c). Particle interfering on image plane is the one passing freely through slits with free space propagation.
- Calculation of inter-plane durations by $t_{j-1,j} = v_z / L_{j-1,j}$ is highly accurate due to $L_{j-1,j} \gg D_{j-1,i}, X_{j-1,i}$ for $j \in [2, N-1]$ and $i \in [-S_j, S_j]$, and setting $L_{0,1}, L_{N-1,N} \gg L_{j-1,j}$ in simulation studies (verified by simulation studies for the effect on detector plane intensity) such that quantum effects are emphasized in x -axis.
- Non-relativistic modeling of particle behavior is assumed since gravitational effects are neglected in proposed dimensions.
- As a proof of concept, source is a single Gaussian wave function while slits are modeled as having Gaussian widths with Feynman's path integral approach [1].

Next, source of quantum computational speed-up is described in comparison with interference architectures utilizing classical waves for quantum search purposes or similar interferometer structures which require exponential resources.

III. ENTANGLED PATH HISTORIES AND WAVE-PARTICLE DUALITY

QC power of universal quantum computers comes from the tensor product structure of Hilbert space leading to entanglement [2, 3, 17, 18]. Entanglement is considered as a special kind of superposition with a product structure on the state space composed of several subsystems while it cannot be represented as a single product state. QPC system design realizes subspaces or *individual qudits* (with multidimensional levels compared with 0-1 qubit representations) as the trajectories through slits on each plane such that the state on j th plane is represented with the ket vector $|x_j\rangle$ as shown in Fig. 1(a). Then, the multiple qudit state right after passing through j th plane denoted by $|\psi_{q,j}\rangle$ is represented as follows:

$$|\psi_{q,j}\rangle \equiv \sum_{x_1=X_{1,-S_1}}^{X_{1,S_1}} \dots \sum_{x_j=X_{j,-S_j}}^{X_{j,S_j}} \alpha(x_1, x_2, \dots, x_j) |x_1 x_2 \dots x_j\rangle \quad (1)$$

where $\alpha(x_1, x_2, \dots, x_j)$ is the amplitude corresponding to path through specific slits denoted by x_1, x_2, \dots, x_j . In the following, the quantum state denoting the trajectory through all $N-1$ planes is denoted by $|\vec{x}_{N-1}\rangle \equiv |x_1 x_2 \dots x_{N-1}\rangle$ while $|\vec{x}_{n,N-1}\rangle$ is the indexed notation with $n \in [0, N_p - 1]$ showing all possible states. It is possible to measure the state on each plane by putting a detector near the slit and checking whether the particle passes through that slit by collapsing the qudit corresponding to that plane to classical states measuring the central points of slit positions. After measurement on j th plane, qudit state $|x_j\rangle$ collapses to one element of multiple level set $X_{j,i}$ for $i \in [-S_j, S_j]$. As the particle travels through slits with increasing time, the amount of information grows exponentially while the state is represented by tensor product of qudit Hilbert spaces on each plane since history of the electron cannot be extracted on previous planes. There is a single particle creating entanglement resource with tensor product in entangled histories compared with traditional multi-particle qubit structures having spatially separated units which are coupled with some entanglement property.

QPC utilizes both the superposition state as in classical wave implementations and also entanglement with the defined tensor product space to calculate a functional output for all

qudit states in polynomial time complexity as shown in Table I in Section VI. Therefore, wave-particle duality as clearly emphasized by Feynman for double-slit experiment is, for the first time, utilized in a compatible way utilizing QC power without explicitly requiring exponential complexity of resources. There is a complete analogy with period finding algorithms in traditional QC algorithms exploiting superposition and entanglement together to realize quantum Fourier transform (QFT) based operations. If we denote $\vec{x}_{n,N-1}$ as $N - 1$ dimensional classical state of slit positions indexed with $n \in [0, N_p - 1]$, then QC power is due to calculating a special function $f(\vec{x})$ defined in Table I with polynomial complexity resources. QPC set-up denoted by *black box* calculates the following form with QC speed-up:

$$\left| \sum_{n=0}^{N_p-1} \gamma_f\left(\frac{T_s}{2\pi} \vec{x}_{n,N-1}, k\right) \left(f\left(\frac{T_s}{2\pi} \vec{x}_{n,N-1}\right)\right)^k \right|^2 = \left| \sum_{n=0}^{N_p-1} \gamma_f\left(\frac{T_s}{2\pi} \vec{x}_{n,N-1}, k\right) f\left(\frac{k T_s}{2\pi} \vec{x}_{n,N-1}\right) \right|^2 \quad (2)$$

where k is an integer, T_s is a pre-defined sampling interval and $\gamma_f(\vec{x}, k)$ is another function whose parameters depend on the specific QPC set-up and defined in Section VI.

In an analogical manner, QPC is different compared with previous formulations based on classical optics [2–5] or interferometer structures [6–16] since they generally do not separate their systems into sub-systems and require exponentially large resources on the order of N_p . QPC requires $\log_{S_T} N_p = N - 1$ planes analogical to $N - 1$ multi-particle qudit formation (assuming each plane includes S_T slits). Classical optics or interference based architectures utilize wave-properties in combination with power of quantum superposition while they lack QC power obtained due to particle property of electrons or photons. QPC achieves to realize tensor product subspaces by utilizing multi-planes and parallel computation of the black box function based on the unique formulation of Feynman’s path integral formalism in combination with Gaussian slits simplifying integral output functions. Therefore, QPC set-up is completely different compared with a simple isomorphism between N_p states of a single particle. It achieves to realize N_p states of $N - 1$ separate qudits with entangled path histories through slits. The proposed system design presents a novel tool to realize QC architectures with single particles and entanglement distributed in time domain. It exploits wave-particle duality in a simple interference set-up rather than utilizing spatially separated multiple particle qubit representations. However, it is definitely necessary to utilize multiple electrons consecutively to sample the interference pattern on the detector screen in a similar manner to the boson sampling [26, 27]. The extension of the proposed set-up by utilizing tools of operator formalism of entangled histories in recent works promises

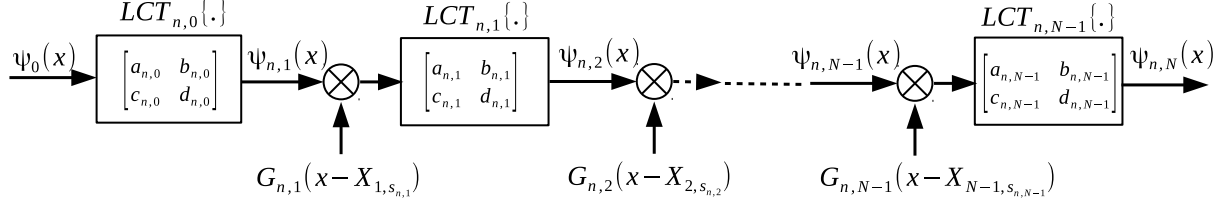


FIG. 2. The representation of evolution of the source wave function $\Psi_0(x)$ in n th path as consecutive operations of $LCT_{n,0}\{\cdot\}$ followed by the operations of $LCT_{n,k}\{\cdot\}$ and multiplication by the effective slit functions $G_{n,j}(x_j)$ for $j \in [1, N-1]$ resulting in the final wave function of $\Psi_{n,N}(x)$.

more interesting QC architectures as future works [19–22]. Next, Feynman’s path integral formalism is utilized to model interference on the screen.

IV. MULTI-PLANE AND MULTI-SLIT EVOLUTION MODELING

Wave function on the detector plane for a specific path index n denoted by $\Psi_{n,N}(x)$ is calculated by using Feynman’s path integrals by using free particle kernels [1]. Assume that $K(x_1, t_1; x_0, t_0) = \sqrt{m / (2\pi i \hbar \Delta t)} \exp(i m \Delta x^2 / (2 \hbar \Delta t))$ denotes free particle kernel for the paths between time-position values (t_0, x_0) and (t_1, x_1) where $\Delta t = t_1 - t_0$ and $\Delta x = x_1 - x_0$, m is the free particle mass and \hbar is the Planck’s constant. Assuming that x_j for $j \in [1, N-1]$ denotes integration variable for the slit with index $s_{n,j}$ and position $X_{j,s_{n,j}}$ in n th path and $\int_{\vec{x}} d\vec{x}$ denotes the integration with respect to the variables x_j for $j \in [0, N-1]$ between limits $-\infty$ and ∞ , then $\Psi_{n,N}(x)$ is given by the following:

$$\begin{aligned} \Psi_{n,N}(x) &= \int_{\vec{x}} K(x, t_N; x_{N-1}, t_{N-1}) G_{n,N-1}(x_{N-1} - X_{N-1,s_{n,N-1}}) \\ &\times \prod_{j=1}^{N-2} K(x_{j+1}, t_{j+1}; x_j, t_j) G_{n,j}(x_j - X_{j,s_{n,j}}) K(x_1, t_1; x_0, t_0) \Psi_0(x_0) d\vec{x} \end{aligned} \quad (3)$$

where $t_j = t_0 + \sum_{k=1}^j t_{k-1,k}$ for $j \in [0, N]$, $G_{n,j}(x_j)$ denotes effective function of the slit with index $s_{n,j}$ on j th plane for n th path, e.g., rectangular or Gaussian slits as described in [1], and $\Psi_0(x_0)$ is the source wave function. The resulting integration is described in terms of linear canonical transforms (LCTs) providing a more intuitive description of the effects of interference on the final wave function for each path. LCT of a function $f(x)$ is defined as

follows [36]:

$$LCT_{a,b,c,d}\{f(x)\} \equiv e^{-i\frac{\pi}{4}}\sqrt{\eta} \int_{-\infty}^{\infty} e^{i\pi(\alpha x^2 - 2\eta x u + \gamma u^2)} f(u) du \quad (4)$$

where LCT matrix is denoted by the following:

$$\begin{bmatrix} a & b \\ c & d \end{bmatrix} = \begin{bmatrix} \frac{\gamma}{\eta} & \frac{1}{\eta} \\ \frac{\alpha\gamma - \eta^2}{\eta} & \frac{\alpha}{\eta} \end{bmatrix} \quad (5)$$

and $ad - bc = 1$ for a given set of parameters (α, γ, η) . Then, it is easily shown that evolution of $\Psi_0(x_0)$ in n th path is represented by the block diagram as shown in Fig. 2 where $LCT_{n,j}\{\cdot\}$ denotes LCT with the following transformation matrix:

$$\begin{bmatrix} a_{n,j} & b_{n,j} \\ c_{n,j} & d_{n,j} \end{bmatrix} = \begin{bmatrix} 1 & \frac{2\pi\hbar t_{j,j+1}}{m} \\ 0 & 1 \end{bmatrix} \quad (6)$$

with the transformation parameters $\alpha = \gamma = \eta = m / (2\pi\hbar t_{j,j+1})$ for $j \in [0, N-1]$ not depending on the path index n due to the classical approximation in z -axis. It is also called as chirp or Fresnel transform in optical signaling literature [36]. The wave function on the boundary of each plane is denoted by $\Psi_{n,j}(x)$ for $j \in [1, N-1]$ while $\Psi_{n,N}(x)$ denotes the final wave function on detector plane. Next, QPC method is presented where superposition interference and entangled path histories of particle are uniquely exploited.

V. QUANTUM PATH COMPUTING

Interfering wave function on image plane is calculated based on Feynman's path integrals and the result is transformed into a form to exploit quantum superposition and parallel computation of black box function for performing computing tasks based on entangled path histories for slit positions. Quantum wave pattern on screen is calculated by using Gaussian beams and slits with the forms of $G_{n,j}(x) = \exp(-x^2 / (2\beta_j^2))$ with identical slits over each plane but with different effective slit widths $D_{j,i} \equiv 2\beta_j$ among the planes, and $\Psi_0(x) = \exp(-x^2 / (2\sigma_0^2)) / \sqrt{\sigma_0\sqrt{\pi}}$ [1, 31]. These assumptions can be replaced with different slit models without modification in the main idea of QPC but resulting into different functional forms of path integrals. After integrating in (3) with Gaussian slits and Gaussian beam sources, following wave function is obtained on j th plane:

$$\Psi_{n,j}(x) = \chi_0 \left(\prod_{k=1}^{j-1} \chi_{n,k} \right) e^{(A_{j-1} + iB_{j-1})x^2 + (C_{n,j-1} + iD_{n,j-1})x} \quad (7)$$

where $j \in [1, N]$, x corresponds to position in x -axis on j th plane and iterative variables $\chi_{n,j}$, A_j , B_j , $C_{n,j}$ and $D_{n,j}$ are defined in Appendix A. Then, resulting wave function $\Psi_{n,N}(x)$ is given by the following with the proof given in Appendix A:

$$\begin{aligned} \Psi_{n,N}(x) = & \chi_0 \left(\prod_{j=1}^{N-1} \sqrt{\xi_j} \right) \exp \left\{ \sum_{k=1}^3 \vec{p}_k^T \left((\mathbf{M}_{1,k} \vec{x}_{n,N-1}) \odot (\mathbf{M}_{2,k} \vec{x}_{n,N-1}) \right) \right\} \\ & \times e^{(A_{N-1} + \imath B_{N-1}) x^2 + (\vec{c}_{N-1}^T + \imath \vec{d}_{N-1}^T) \vec{x}_{n,N-1} x} \end{aligned} \quad (8)$$

where $\mathbf{M}_{1,1} = \mathbf{M}_{2,1} = \mathbf{I}_{N-1}$, $\mathbf{M}_{1,2} = \mathbf{M}_{2,2} = \mathbf{G}$, $\mathbf{M}_{1,3} = \mathbf{G}$, $\mathbf{M}_{2,3} = \mathbf{E}_1$, \mathbf{I}_k is identity matrix of size k , the complex valued matrices \mathbf{G} and \mathbf{E}_1 , real valued column vectors \vec{c}_{N-1} , \vec{d}_{N-1} , complex valued column vectors \vec{p}_k for $k \in [1, 3]$, real valued iterative variables A_j and B_j , and complex valued iterative variable ξ_j are defined in Appendix A, and $\vec{x}_{n,k} = [X_{1,s_{n,1}} X_{2,s_{n,2}} \dots X_{k,s_{n,k}}]^T$. Superposition rule and Born's principle are utilized to find relative intensity distribution on display screen as follows:

$$I(x) = \left| \Psi_N(x) \right|^2 = \left| \sum_{n=0}^{N_p-1} \Psi_{n,N}(x) \right|^2 = \lambda e^{2A_{N-1} x^2} \left| \sum_{n=0}^{N_p-1} e^{r\{\vec{x}_n\}} e^{\vec{c}^T \vec{x}_n x} e^{\imath \vec{d}^T \vec{x}_n x} \right|^2 \quad (9)$$

where the subscript $N-1$ is dropped from the vectors to simplify the notation, e.g., $\vec{x}_n \equiv \vec{x}_{n,N-1}$, $\vec{c} \equiv \vec{c}_{N-1}$ and $\vec{d} \equiv \vec{d}_{N-1}$, $\lambda \propto |\chi_0 \prod_{j=1}^{N-1} \sqrt{\xi_j}|^2$ is some constant regarding the amount of intensity on screen depending on the set-up and electron beam intensity, and $r\{\vec{x}_n\} \equiv \sum_{k=1}^3 \vec{p}_k^T ((\mathbf{M}_{1,k} \vec{x}_n) \odot (\mathbf{M}_{2,k} \vec{x}_n))$. It can be easily shown that $r\{\vec{x}_n\}$ is equal to $\vec{x}_n^T \mathbf{H} \vec{x}_n$ where the proof is given in Appendix B and the matrix \mathbf{H} is given by the following:

$$\mathbf{H} = \sum_{k=1}^3 \mathbf{M}_{2,k}^T \text{diag}\{\vec{p}_k\} \mathbf{M}_{1,k} \quad (10)$$

where $\text{diag}\{\vec{y}\}$ is the operator creating a diagonal matrix with diagonal elements composed of the vector \vec{y} . Then, assuming that intensity distribution normalized by $1/\lambda$ is denoted by $I_{norm}(x)$, the resulting pattern measured on screen depending on resolution of the measurement apparatus is given by the following:

$$I_{norm}(x) = e^{2A_{N-1} x^2} \left| \sum_{n=0}^{N_p-1} e^{\vec{x}_n^T \mathbf{H}_R \vec{x}_n} e^{\imath \vec{x}_n^T \mathbf{H}_I \vec{x}_n} e^{\vec{c}^T \vec{x}_n x} e^{\imath \vec{d}^T \vec{x}_n x} \right|^2 \quad (11)$$

where $\mathbf{H} = \mathbf{H}_R + \imath \mathbf{H}_I$ is composed of correlated real \mathbf{H}_R and imaginary parts \mathbf{H}_I extracted from (10). This is the main equation where computational power of QPC resides. The combined design of \vec{x}_n , \mathbf{H} , \vec{c} , \vec{d} and A_{N-1} by choosing specific set of x -axis samples promises

a solution to a significant number of optimization problems including huge memory and time complexities with significantly large N_p . Quantum superposition in measurement provides information about collective behavior of \mathbf{H} , $\vec{\mathbf{c}}$ and $\vec{\mathbf{d}}$ for exponentially large number of sample vectors $\vec{\mathbf{x}}_n$ with a summation over them. Assuming that $N_p = (2S_0 + 1)^{N-1}$ where $S_j = S_0$ for $j \in [1, N-1]$, then a single measurement at the sample position x provides information about collective result of $(2S_0 + 1)^{N-1} \times (N-1)$ multiplications performing $\vec{\mathbf{d}}^T \vec{\mathbf{x}}_n$ for $n \in [0, N_p - 1]$. Similar to QC algorithms exploiting superposition, e.g., period finding solutions for *hidden subgroup problems (HSPs)* [37], a clever way is necessary to best utilize QPC power of (11) as provided in the next section.

The number of degrees of freedom to tailor the matrices for a general QPC set-up is $\sum_{j=1}^{N-1} S_{j,T} + N + (N-1) + 1 = \sum_{j=1}^{N-1} S_{j,T} + 2N$ where the first summation term is due to distinct positions of slits on each plane, the term N due to the number of inter-plane distances, the term $N-1$ due to different slit widths β_j for $j \in [1, N-1]$ and the last term due to σ_0 . In the following sections, a specific QPC set-up refers to the tuned parameters of $\vec{\beta}$, $\vec{\mathbf{L}}$, σ_0 and T_s for the specific grid \mathbf{X}_{N-1} forming the vectors $\vec{\mathbf{x}}_n$ for $n \in [0, N_p - 1]$ and vector $\vec{\mathbf{d}}$ defining the number theoretic problem where T_s refers to sampling period on detector plane. Next, QPC framework is utilized to solve HSP for periodicity of $e^{i2\pi \vec{\mathbf{d}}^T \vec{\mathbf{x}}}$ with respect to $\vec{\mathbf{x}}$ or SDA problem for the set of real numbers which are $(2\pi)^{-1} T_s$ scaled versions of $\vec{\mathbf{d}}^T \vec{\mathbf{x}}_n$ for $n \in [0, N_p - 1]$.

VI. HIDDEN SUBGROUPS AND NON-UNIFORM LATTICES

QC algorithms exploit superposition state generated with quantum Hadamard transforms applied on two registers initially at $|\mathbf{0}\rangle |\mathbf{0}\rangle$ and evolution with controlled unitary transforms U in black boxes for a given periodic function $f(x) = f(x + r)$ [37]. QPC equation in (11) allows to find periodicities in $f(\vec{\mathbf{x}}) \equiv e^{i2\pi \vec{\mathbf{d}}^T \vec{\mathbf{x}}}$ as a complex problem for arbitrary sets of \mathbf{X}_{N-1} and $\vec{\mathbf{d}}$ as defined in the following problem definitions and Table I which is explained in detail after intensity formulation and problem definitions. The continuous intensity is renormalized and sampled by defining $\tilde{I}[k] \equiv I_{norm}[k] e^{-2A_{N-1}(kT_s)^2}$ as follows:

$$\tilde{I}[k] \equiv \left| \sum_{n=0}^{N_p-1} \gamma_f\left(\frac{T_s}{2\pi} \vec{\mathbf{x}}_n, k\right) f\left(\frac{kT_s}{2\pi} \vec{\mathbf{x}}_n\right) \right|^2 \equiv \left| \sum_{n=0}^{N_p-1} e^{\vec{\mathbf{x}}_n^T (\mathbf{H}_{\mathbf{R}}) \vec{\mathbf{x}}_n} e^{\vec{\mathbf{c}}^T \vec{\mathbf{x}}_n k T_s} e^{i\Theta[n,k]} \right|^2 \quad (12)$$

TABLE I. The analogy between QC and QPC period finding algorithms

Steps	QC Period Finding Algorithm [37]		QPC Period Finding Algorithm	
	Procedure	# Ops.	Procedure	# Ops.
0	a. The function $f(x)$ b. x is integer, producing single bit output c. Periodic for $0 < r < 2^L$ integer: $f(x) = f(x+r)$ d. Black box performing $U x\rangle y\rangle = x\rangle y \oplus f(x)\rangle$	0	a. The function $f(\vec{x}) = e^{i2\pi\vec{d}^T\vec{x}}$, \vec{x} and \vec{d} are tunable real vectors by the set-up b. The basis periodicity sets defined as $S_a : \{\vec{r}_a = \sum_{n=0}^{N_p-1} a_n \vec{x}_n^s, a_n \in \mathbb{Z}, n \in [0, N_p - 1]\}$ for $\vec{x}_n^s \in \mathbf{X}_{N-1}^s$ c. $f(\vec{x}) = f(\vec{x} + \tilde{k} \vec{r}_a)$ with the sets $S_{\tilde{k}} : \{\tilde{k} \vec{r}_a, \vec{r}_a \in S_a\}$ d. QPC set-up or black box performing $f(k \vec{x}_n^s)$ given the input \vec{x}_n^s and integer k	0
1	Initial state: $ \mathbf{0}\rangle \mathbf{0}\rangle$	0	$ \Psi_0\rangle, \Psi_0(x)$ formed as a simple Gaussian electron beam	0
2	Superposition: $\frac{1}{\sqrt{2^t}} \sum_0^{2^t-1} \mathbf{x}\rangle \mathbf{0}\rangle$	0	N_p paths to reach the detector with \vec{x}_n^s for $n \in [0, N_p - 1]$ and $\sum_{n=0}^{N_p-1} \vec{x}_n^s\rangle \Psi_0\rangle$	0
3	Black box $U: \frac{1}{\sqrt{2^t}} \sum_0^{2^t-1} \mathbf{x}\rangle f(\mathbf{x})\rangle$	1	Black box with parameters $\mathbf{X}_{N-1}^s, \vec{\beta}, \vec{L}$ and σ_0 : $\Psi_N(kT_s) = \sum_{n=0}^{N_p-1} \Psi_{n,N}(kT_s)$ $\propto \sum_{n=0}^{N_p-1} \gamma_f(\vec{x}_n^s, k) f(k \vec{x}_n^s)$	1
4 & 5	a. IQFT: $\frac{1}{\sqrt{r}} \sum_0^{r-1} \widetilde{l/r}\rangle \widetilde{f(l)}\rangle$ b. Measure first register: $\widetilde{l/r}$	$O(L^2)$	a. Measure $ \Psi_N(kT_s) ^2$ at various k values b. Perform $IFFT_M$ at p with $M \geq \tilde{k} : \sum_{h=0}^{\tilde{k}-1} \Gamma_M[\frac{p}{M}, \frac{h}{k}]$	$O(M \log M)$
6	Continued fractions: r	$O(L^3)$	Check IFFT at $p \in [0, M - 1]$ values for $M \geq \tilde{k}$ providing an estimation for h/\tilde{k} for $h \in [0, \tilde{k} - 1]$ and resulting in a converging estimation of \tilde{k}	Polynomial complexity

where the measurement location x is represented in terms of samples kT_s for integer indices $k \in [-\infty, \infty]$ and sampling period T_s , and $\gamma_f(\vec{x}, k)$ and $\Theta[n, k]$ are defined as follows:

$$\gamma_f(\vec{x}, k) \equiv e^{\frac{4\pi^2}{T_s^2} \vec{x}^T \mathbf{H} \vec{x}} e^{2\pi \vec{c}^T \vec{x} k} \quad (13)$$

$$\Theta[n, k] \equiv \vec{x}_n^T \mathbf{H}_I \vec{x}_n + \vec{d}^T \vec{x}_n k T_s \quad (14)$$

The analogy between QC (the algorithm in Section 5.4.1 in [37]) and QPC period finding is shown in Table I explained in detail after defining the following computational problems:

Problem 1 Periodicity detection and reciprocal lattice of a non-uniform lattice:
Find the minimum integer $\tilde{k} \in \mathbb{Z}^+$ scaling a given $N - 1$ dimensional real vector \vec{d} for a given non-uniform lattice denoted by \mathbf{X}_{N-1}^s (scaled with respect to \mathbf{X}_{N-1}) resulting in a reciprocal integer lattice denoted by Λ by minimizing the error term ϵ_n for $n \in [0, N_p - 1]$

in a defined average sense such that $\Lambda \equiv \{\tilde{k} \vec{d}^T \vec{x}_n^s + \epsilon_n \in \mathbb{Z}; \forall \vec{x}_n^s, n \in [0, N_p - 1]\}$ where non-uniform lattice \mathbf{X}_{N-1}^s formed of a set of real vectors \vec{x}_n^s is defined as follows:

$$\vec{x}_n^s = (2\pi)^{-1} T_s [\vec{x}_n(1) \dots \vec{x}_n(N-1)] \text{ with } \vec{x}_n(j) \in \{X_{j,-S_j}, \dots, X_{j,S_j}\}$$

$$\text{s.t. } X_{j,i} - X_{j,i+1} > 2\alpha\beta_j; N \geq 2; \alpha \geq 1; N_p \equiv \prod_{j=1}^{N-1} (2S_j + 1) \quad (15)$$

where $n \in [0, N_p - 1]; j \in [1, N - 1]; i \in [-S_j, S_j - 1]$

$$S_j, N \in \mathbb{Z}^+; \beta_j, T_s, \alpha \in \mathbb{R}^+; X_{j,i} \in \mathbb{R}$$

where $\mathbb{Z}, \mathbb{Z}^+, \mathbb{R}$ and \mathbb{R}^+ denote the sets of integers, positive integers, real values and positive real values, respectively.

Optimization problem defined in Problem 1 requests defining a set of integers scaling either \vec{d} or \mathbf{X}_{N-1}^s such that inner product of \vec{d} with all vectors in \mathbf{X}_{N-1}^s results in values very close to integers with errors given by ϵ_n . The condition $X_{j,i} - X_{j,i+1} > 2\alpha\beta_j$ satisfies that central positions of two slits are separated by the distance at least as much as the summation of their half widths where increasing α results in better physical design to satisfy Gaussian slit properties. The other conditions are definitions of parameters of physical set-up described in Sections IV and V. Similarly, a parallel problem, i.e., SDA problem with NP-hard complexity modeled in [35], is defined as follows:

Problem 2 Simultaneous Diophantine approximation: *Decide the existence and find the minimum integer $\tilde{k} \in \mathbb{Z}^+$ where $\tilde{k} \leq K_{pre}$ for some predefined $K_{pre} \in \mathbb{Z}^+$ such that it is SDA solution for the set of real numbers in the set $S_b = \{b_0, b_1, \dots, b_{N_p-1}\}$ satisfying the relation $|\tilde{k}b[n] - k_n| < \epsilon$ for $n \in [0, N_p - 1]$ and for some $k_n \in \mathbb{Z}$ specific to each n with the common denominator \tilde{k} where $b[n] \equiv \vec{d}^T \vec{x}_n^s$ and ϵ is the bound.*

The first problem requires inner product multiplications for $\prod_{j=1}^{N-1} S_{j,T}$ different \vec{x}_n^s values and more difficultly rationalizing the resulting values. Reciprocal lattices are well defined for Bravais lattices where the crystal structure is defined by a transformation vector. On the other hand, quasicrystals or crystals with non-uniform set of grid points are more difficult to analyze due to the lack of the strict order but rather repeating patterns [38]. In the current case, $N - 1$ dimensional lattice \mathbf{X}_{N-1}^s has not any periodicity assumption (the reason to denote as *non-uniform lattice*) such that it is the intersection of $N - 1$ sets of planes where the number of planes in each dimension $j \in [1, N - 1]$ is equal to $S_{j,T}$ and planes are

separated in the dimension denoted with the position x_j without any defined periodicity or pattern.

The equivalent second problem is NP-hard as discussed in [35] and it is assumed that inner product set of $\vec{d}^T \vec{x}_n^s$ for $n \in [0, N_p - 1]$ achieves the desired set of real numbers $b[n]$ by tuning physical system set-up parameters in QPC solution. The transformation mapping an arbitrary SDA problem to the physical set-up parameters is left as a future work to be achieved based on the fundamental model in this article.

Problems 1 and 2 are solved by utilizing (11-14) in combination with a set of measurements at $x = k T_s$ as shown in the next sections. The steps of the proposed QPC algorithm are described as follows while the analogy with QC period finding is shown in Table I:

0. Real vector \vec{d} and real grid \mathbf{X}_{N-1} with elements \vec{x}_n for $n \in [0, N_p - 1]$ are given where $\vec{x}_n \equiv [X_{1,s_{n,1}} X_{2,s_{n,2}} \dots X_{k,s_{n,N-1}}]^T$ and \mathbf{X}_{N-1} is composed of the positions $X_{j,i}$ for $j \in [1, N - 1]$ and $i \in [-S_j, S_j]$. The function $f(\vec{x}) = e^{i 2 \pi \vec{d}^T \vec{x}}$ has periodicity with respect to \vec{x} with the unknown period \tilde{k} and the given basis sets $S_a : \{\vec{r}_a = \sum_{n=0}^{N_p-1} a_n \vec{x}_n^s, a_n \in \mathbb{Z}, n \in [0, N_p - 1]\}$ while periodicity vector is given by $\tilde{k} \sum_{n=0}^{N_p-1} a_n \vec{x}_n^s$ for any $a_n \in \mathbb{Z}$ and $n \in [0, N_p - 1]$, and the target is to find \tilde{k} where $\vec{x}_n^s \equiv (2 \pi)^{-1} T_s \vec{x}_n$. Black box is formed of QPC set-up with the ability to measure intensity and perform $f(k \vec{x}_n^s)$ given the input \vec{x}_n^s and integer k .
1. Initial state $|\Psi_0\rangle$ is set up by designing wave function of the particle source.
2. The superposition is due to QPC set-up combining N_p different paths on the screen with the initial state $\sum_{n=0}^{N_p-1} |\vec{x}_n^s\rangle |\Psi_0\rangle$.
3. Black box is the QPC set-up with specially designed parameters providing \vec{x}_n in the grid \mathbf{X}_{N-1} and the vector \vec{d} while related parameters \vec{c} , \mathbf{H} , and the set-up parameters $\vec{\beta}$, \vec{L} , σ_0 and T_s to be optimally designed for generating \vec{x}_n^s and the best estimation of \tilde{k} . It performs $\Psi_N(k T_s) \propto \sum_{n=0}^{N_p-1} \gamma_f(\vec{x}_n^s, k) f(k \vec{x}_n^s)$ for integer k .
- 4 & 5 A set of $M \geq \tilde{k}$ samples are taken on detector plane and IFFT operation with complexity $O(M \log M)$ with the output time index p results in information about p / \tilde{k} and h / \tilde{k} for $h \in [0, \tilde{k} - 1]$ where $\Gamma_M[\frac{p}{M}, \frac{h}{k}]$ is in (20).

6 The number of samples at varying p values is increased for a converging and unbiased estimation of \tilde{k} . The estimation problem can be set as a parameter estimation problem for the set of damped sinusoids with diverging coefficients or the estimation can be made easier if the set-up satisfies some special properties as described in the following sections. Traditional period finding algorithms with polynomial time solutions are utilized to best estimate \tilde{k} , i.e., $O(M \log M)$ complexity for FFT based solutions in frequency estimation of damped sinusoids [39].

IFFT operation with the number of samples M described in Step-4&5 is given as follows by using (12). Define the following discrete functions of n as $g_1[n] \equiv \tilde{\mathbf{c}}^T \tilde{\mathbf{x}}_n T_s$, $g_2[n] \equiv \tilde{\mathbf{d}}^T \tilde{\mathbf{x}}_n T_s$ and $g_3[n] \equiv e^{\tilde{\mathbf{x}}_n^T \mathbf{H} \tilde{\mathbf{x}}_n}$. Since $\tilde{\mathbf{d}}$ and $(2\pi)^{-1} T_s \tilde{\mathbf{x}}_n$ form an integer lattice for $n \in [0, N_p - 1]$ with integer period \tilde{k} , the expression $e^{i g_2[n] k}$ is simplified by $e^{i \tilde{G}_2[n] 2\pi k / \tilde{k}}$ due to periodicity with \tilde{k} where $\tilde{G}_2[n]$ is a function mapping the interval $[0, N_p - 1]$ into an integer between $[0, \tilde{k} - 1]$ depending on relation between $\tilde{\mathbf{d}}$ and \mathbf{X}_{N-1}^s . Then, if $IFFT\{Y\}[p]$ denotes IFFT of some discrete function $Y[k]$ at the time index p , IFFT with size M by utilizing $k \in [0, M - 1]$ results in the following:

$$IFFT_M\{\tilde{I}\}[p] \equiv \frac{1}{\sqrt{M}} \sum_{k=0}^{M-1} \sum_{n=0}^{N_p-1} \sum_{l=0}^{N_p-1} g_3[n] g_3^*[l] e^{(g_1[n] + g_1[l])k} e^{-\frac{i 2\pi k (\tilde{G}_2[l] - \tilde{G}_2[n])}{\tilde{k}}} e^{\frac{i 2\pi k p}{M}} \quad (16)$$

$$= \sum_{n=0}^{N_p-1} \sum_{l=0}^{N_p-1} \frac{1}{\sqrt{M}} A[n, l] \frac{1 - \gamma_{n,l,p}^M}{1 - \gamma_{n,l,p}} \quad (17)$$

where $\gamma_{n,l,p}$ is defined as follows:

$$\gamma_{n,l,p} \equiv e^{\alpha[n,l]} e^{-\frac{i 2\pi}{M \tilde{k}} (\Delta G_2[n,l] M - p \tilde{k})} \quad (18)$$

where diverging coefficients are $\alpha[n, l] = g_1[n] + g_1[l]$, amplitudes $A[n, l] = g_3[n] g_3^*[l]$ and the set of multiplying coefficients of $\omega_0 \equiv 2\pi / \tilde{k}$ is $\Delta G_2[n, l] = \tilde{G}_2[l] - \tilde{G}_2[n] \in [-\tilde{k} + 1, 2\tilde{k} - 2]$. Dividing the set of $[n, l]$ pairs in $[0, N_p - 1] \times [0, N_p - 1]$ into \tilde{k} regions with index $h \in [0, \tilde{k} - 1]$ and denoted by R_h results in the following:

$$IFFT_M\{\tilde{I}\}[p] = \sum_{h=0}^{\tilde{k}-1} \Gamma_M\left[\frac{p}{M}, \frac{h}{\tilde{k}}\right] \quad (19)$$

where $\text{mod}(\Delta G_2[n, l], \tilde{k}) = h$ and $\Gamma_M[\frac{p}{M}, \frac{h}{\tilde{k}}]$ is as follows:

$$\Gamma_M\left[\frac{p}{M}, \frac{h}{\tilde{k}}\right] = \sum_{n,l \in R_h} \frac{1}{\sqrt{M}} A[n, l] \frac{1 - e^{\alpha[n,l] M} e^{-i 2\pi \frac{h M}{\tilde{k}}}}{1 - e^{\alpha[n,l]} e^{-i 2\pi (\frac{h}{\tilde{k}} - \frac{p}{M})}} \quad (20)$$

Furthermore, if $M = \tilde{k}$, the following is obtained:

$$\Gamma_{\tilde{k}}[\frac{p}{\tilde{k}}, \frac{h}{\tilde{k}}] = \sum_{n,l \in R_h} \frac{1}{\sqrt{\tilde{k}}} A[n, l] \frac{1 - e^{\alpha[n,l] \tilde{k}}}{1 - e^{\alpha[n,l] e^{-\frac{\iota 2\pi}{\tilde{k}}(h-p)}}} \quad (21)$$

Then, if novel mathematical tools are designed utilizing $g_3[n]$ and $g_1[n]$ for computationally efficient estimation of \tilde{k} , each sample point on detector plane increases estimation accuracy. Similar to the Bertocco algorithm for the single sinusoid case [39], it is observed that exponentially increasing term in the numerator, i.e., $1 - e^{\alpha[n,l] M e^{-\frac{\iota 2\pi}{\tilde{k}}(h-p)}}$, results in fast phase oscillations for each $h \in [0, \tilde{k} - 1]$ if $M < \tilde{k}$. Various performance metrics are capable of detecting high fluctuations, e.g., the following metric denoted by $R[M]$ is expected to be maximized around $M \approx \tilde{k}$ as a polynomial complexity solution:

$$R[M] = \frac{|IFFT_M\{\tilde{I}\}[0]|}{\frac{1}{M-1} \sum_{k=1}^M |IFFT_M\{\tilde{I}\}[k]|} \quad (22)$$

where high frequency components are averaged and their mean is compared with zero frequency component. Then, by checking the samples of $R[M]$ with respect to M , i.e., minimizing high frequency components, allows roughly determining \tilde{k} . On the other hand, the same periodicity is expected in $R[M]$ since fluctuations are decreased at multiples of \tilde{k} . Next, solution of SDA problem with QPC algorithm is proposed.

A. QPC Solution of SDA Problem

Existence of $\tilde{k} \leq K_{pre} \equiv M$ is checked by the existence of high fluctuation points in solution of particular SDA problem defined in Problem 2. If there is no fluctuation, it is an indication of absence of the bounded error ϵ such that solution of SDA problem does not exist for $k \leq M$. On the other hand, if there is a fluctuation, the set of fluctuating points are the best candidates for SDA solution periods and it is necessary to test them and chose the best result. Moreover, classical period finding algorithms with polynomial computational complexity are promising to find periodicity if it exists [39]. However, formal mathematical proof for the decision of SDA solution existence depending on more detailed models of \vec{d} and \mathbf{X}_{N-1} combined with \mathbf{H} and \vec{c} in (11) is left as a future work providing the metric for fluctuation compared with other values in interval $1 \leq k \leq M$ to decide in favor of the existence of SDA solution. Furthermore, the set of SDA problems whose

solutions are achieved by a specific QPC set-up should be mathematically modeled. In this article, example problems are simulated as a proof of concept promising future system designs providing QPC solutions to specific sets of SDA problems.

Besides that, polynomial solutions of SDA problem and performance of the well defined Lenstra, Lenstra Jr., and Lovasz (LLL) algorithm for large number of inputs become highly prohibitive for $N_p \gg 1$ [35]. Assume that $\|x\|$ denotes the distance of the real number x to the closest integer, the maximum of $\|\tilde{k}b[n]\|$ for $n \in [0, N_p - 1]$ is smaller than some pre-defined ϵ_p and there is some pre-defined bound M with $M > \tilde{k}$. Then, LLL algorithm provides estimation of \tilde{k} denoted by \hat{k} satisfying $1 < \hat{k} < 2^{N_p/2} M$ and the maximum of $\|\hat{k}b[n]\|$ being smaller than $\sqrt{5N_p} 2^{(N_p-1)/2} \epsilon_p$ with the number of operations depending on input size [35]. Therefore, QPC algorithm not only promises a powerful approach as a candidate to solve specific instances of the problem for the decision of SDA solution existence and to find it but also improves existing polynomial solution approaches requiring significant time steps and memory with a limited accuracy.

Error term for SDA problem is defined as $\epsilon[n, M] \equiv \min\{\|Mb[n]\|\}$ for $n \in [0, N_p - 1]$. Then, $\bar{\epsilon}[M] \equiv (1/N_p) \sum_{n=0}^{N_p-1} \epsilon[n, M]$, $\epsilon_{max}[M] \equiv \max_n \{\epsilon[n, M]\}$ and $\epsilon_{min}[M] \equiv \min_n \{\epsilon[n, M]\}$ are good indicators for observing how M is close to the solution of SDA problem, i.e., \tilde{k} . Formal mathematical proof of modeling the family of problems requires more analysis as a future work. On the other hand, although the accuracy of the digits of the SDA solution can be increased, there is potentially a limit to the accuracy due to combined effects of physical parameters including \hbar , π , and inaccuracies in Gaussian source, coordinates of the physical locations, distances of the planes, widths of the slits and plane thicknesses requiring further work on the highest accuracy of solving a specific SDA problem. Therefore, specific number theoretic problems should be converted to a model where minimizing $\bar{\epsilon}[M]$ should give an acceptable solution.

In the following chapters, two different approaches are also introduced which may become more effective, i.e., utilizing special property of $g_3[n]$ and $g_1[n]$ resulting in periodicity in the local maximum of $\tilde{I}[k]$ and considering the problem as fundamental frequency estimation for a sum of sinusoids. Estimation under heavy noise on screen requires more advanced methods to extract periodicity. However, accuracy of IFFT method can be increased by diversity combining methods, e.g., increasing signal-to-noise ratio (SNR) in each sample point and realizing multiple experiments consecutively or in parallel.

B. Periodicity Detection in Intensity Local Maximum

Assume that non-uniform lattice \mathbf{X}_{N-1}^s and vector $\vec{\mathbf{d}}$ are in a specific family providing the conditions defined in Theorem 1 as follows:

Theorem 1 Assume that $N - 1$ dimensional real vectors $\vec{\mathbf{c}}$ and $\vec{\mathbf{d}}$, and a non-uniform grid \mathbf{X}_{N-1} satisfy the following while constructing intensity $\tilde{I}[k]$ defined in (12):

1. $\vec{\mathbf{d}}$ and \mathbf{X}_{N-1}^s form an integer lattice with the integer period \tilde{k} and sampling interval T_s allowing the simplification of the expression $e^{i g_2[n] k} = e^{i \vec{\mathbf{d}}^T \vec{\mathbf{x}}_n T_s k}$ by $e^{i \tilde{G}_2[n] 2 \pi k / \tilde{k}}$.
2. $|H[k, \tilde{G}_2]| < |H[k, 0]|$ and $|H[k_1, 0]| > |H[k_2, 0]|$ where $0 \leq k \leq \tilde{k}$, $k_2 < k_1 \leq \tilde{k}$, and $k, k_1, k_2 \in \mathbb{Z}$, and $H[k, o]$ is defined as follows:

$$H[k, o] \equiv \sum_{n=0}^{N_p-1} g_3[n] e^{g_1[n] (\tilde{k}-k)} e^{-i \frac{2 \pi o[n] k}{\tilde{k}}} \quad (23)$$

where $o[n] \in [0, \tilde{k} - 1]$ refers to a specific mapping of $n \in [0, N_p - 1]$ with a discrete function $o(\cdot)$ while $H[k, 0]$ refers to the case where $o(n) = 0$. Then, the following is satisfied for $k \in [0, \tilde{k} - 1]$:

$$\tilde{I}[\tilde{k}] > \tilde{I}[k] \quad (24)$$

The proof is provided in Appendix C. Then, periodicity \tilde{k} is heuristically found by checking local maximums in intensity. Formal proof and the algorithm for finding solutions for the general class of problems are left as future works. Checking local maximum points \hat{k} with random samples of $\vec{\mathbf{d}}^T \vec{\mathbf{x}}_n \hat{k} T_s / (2 \pi)$ to verify for integer values determines periodicity \tilde{k} . However, performance can be increased by using various methods for frequency estimation of damped sinusoids as described in [39] such as FFT based ones as shown next.

C. Periodicity Estimation for Diverging Sinusoids with Fundamental Frequency

The problem is considered as finding the fundamental frequency $\omega_0 = 2 \pi / \tilde{k}$ for the summation of complex sinusoidal signals if (12) is transformed into the following:

$$\tilde{I}[k] = \sum_{n=0}^{N_p-1} \sum_{l=0}^{N_p-1} A[n, l] e^{\alpha[n, l] k} e^{-i \Delta G_2[n, l] \omega_0 k} \quad (25)$$

Received intensity in noisy receiver case denoted by $I_{norm,n}[k]$ is modeled as follows:

$$I_{norm,n}[k] = I_{norm}[k] + n[k] \quad (26)$$

where $n[k]$ is the receiver noise modeled as Gaussian random process with independent samples and with the variance σ_k^2 which becomes proportional to $I_{norm}[k]$ if Poisson distribution is assumed for photonic applications. However, in simulation studies, various levels of SNR are simulated. Then, normalized intensity is found as follows where noise is amplified in normalization operation:

$$\tilde{I}_n[k] = \tilde{I}[k] + \tilde{n}[k] \quad (27)$$

where $\tilde{n}[k] = e^{-2 A_{N-1} (k T_s)^2} n[k]$ with the variance $\tilde{\sigma}^2[k] \equiv e^{-4 A_{N-1} (k T_s)^2} \sigma_k^2$ and $\sigma_k^2 \leq \sigma_{max}^2$.

On the other hand, Cramer-Rao lower bound for the variance of the best estimate of \tilde{k} in noisy receiver case is provided in the following theorem which is useful to find performance of the best estimator:

Theorem 2 *Cramer-Rao lower bound for the estimation of periodicity in reciprocal integer lattice of QPC set-up by using a set of intensity measurements on screen in M different positions with sample points $k_p T_s$ for $p \in [0, M - 1]$ is given as follows:*

$$CRB(\tilde{k}) = \frac{(1 + \delta b(\hat{k}) / \delta \hat{k})^2}{\sum_{p=0}^{M-1} \left(\frac{1}{\tilde{\sigma}[p]} \frac{\delta \tilde{I}[k_p]}{\delta \tilde{k}} \right)^2} \quad (28)$$

where $b(\hat{k}) \equiv E\{\hat{k}\} - \tilde{k}$ is the bias while noise is assumed to have zero mean.

The proof is provided in Appendix D. Next, effects of exotic paths discussed in [31–34] are analyzed by extending previous formulations to include effects of all possible exotic paths on detector plane.

VII. EFFECTS OF EXOTIC PATHS

Evolved wave function is calculated by summing contributions from both classical (denoting the paths not including trajectories on a single plane with the distinction made by the recent studies [31–34]) and exotic paths (trajectories including visitings on a single plane) by providing a complete formulation of QPC set-up. A sample exotic path is shown in Fig.

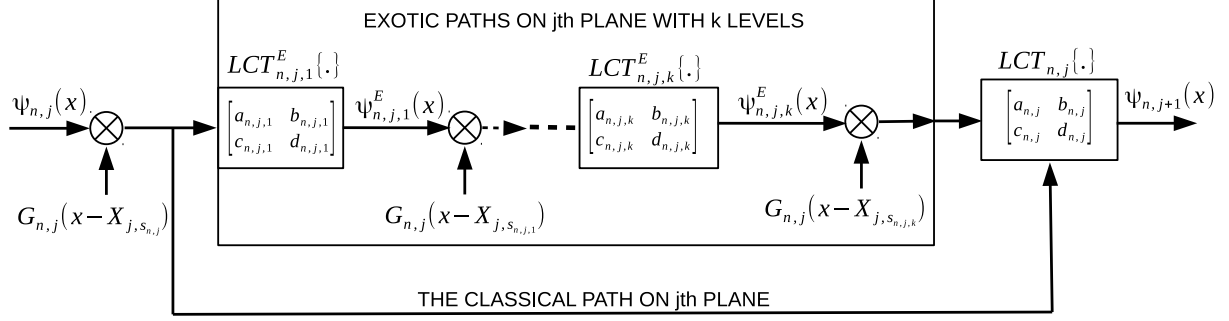


FIG. 3. The representation of evolution of source wave function $\Psi_{n,j}(x)$ on j th plane in n th path as consecutive operations of exotic movements $LCT_{n,j,i}^E\{\cdot\}$ followed by multiplication of $G_{n,j}(x - X_{j,s_{n,j,i}})$ for $i \in [1, k]$ resulting in $\Psi_{n,j+1}(x)$.

1(c). Assume that the particle of n th path on j th plane makes k consecutive visits to slits in addition to the first slit or the entrance slit with the index $s_{n,j}$ and position $X_{j,s_{n,j}}$ while the case with $k = 0$ corresponds to classical path as shown in Fig. 3. Block diagram of evolution of the wave function in n th path is shown where the path is either a classical or an exotic path denoted with the same notations of $\Psi_{n,j}(x)$ and $\Psi_{n,j+1}(x)$ on j th and $j + 1$ th planes, respectively. The wave function in the exotic path after k th slit denoted by $\Psi_{n,j,k}^E(x)$ is explicitly provided in Appendix E for k bounded by some predetermined maximum number N_E . The parameters of $LCT_{n,j,k}^E\{\cdot\}$ depend on the distance between the slits on j th plane defined as $\Delta_x^E(j, k) \equiv |X_{j,s_{n,j,k}} - X_{j,s_{n,j,k-1}}|$ where $X_{j,s_{n,j,k}}$ denotes the central position of k th visited slit and $k = 0$ case corresponds to the position of the first slit on j th plane, i.e., $X_{j,s_{n,j,0}} \equiv X_{j,s_{n,j}}$. Then, setting a maximum for N_E and finding all paths for $k \in [0, N_E]$ give an accurate result considering effects of all possible exotic paths.

Operator formalism for calculating Gouy phase in [31] is utilized to calculate time durations for the path distance $\Delta_x^E(j, k)$ with $t_{k-1,k}^E(j) \equiv \Delta_x^E(j, k) / \Delta_v^E(j) = m \Delta_x^E(j, k) / \Delta_p^E(j)$ where $\Delta_p^E(j) = \sqrt{\langle p^2 \rangle - \langle p \rangle^2}$ and $\langle p^a \rangle$ for $a \in [1, 2]$ is defined as follows:

$$\langle p^a \rangle \equiv \int_{-\infty}^{\infty} \Psi_j^*(x) \left(\frac{\hbar}{i} \frac{\delta}{\delta x} \right)^a \Psi_j(x) dx \quad (29)$$

where $\Psi_j(x)$ is the total wave function on j th plane as a superposition of all previous paths. Total number of different paths between j th and $(j+1)$ th planes including exotic movements is denoted by $N_{e,j}$ which is calculated by the following formulation:

$$N_{e,j} = S_{j,T} \sum_{k=1}^{N_E} (S_{j,T} - 1)^k \quad (30)$$

while total number of all paths on i th plane for $i \in [1, N]$ is given by $N_{p,i}^E \equiv \prod_{j=1}^{i-1} N_{e,j}$. Total number of paths on image plane is denoted by $N_{p,N}^E$ which is much larger compared with the case including only classical paths, i.e., N_p , and total number of contributions and effects of the exotic paths are simulated in Section VIII for the proposed sample problems. The first term $S_{j,T}$ shows different selections of the entrance slit while remaining k different slit visitings occur in $(S_{j,T} - 1)^k$ permutations. Finally, summing the contributions for different k values until N_E results in (30). In the next section, numerical simulations are performed for two different SDA problems as a proof of concept.

VIII. NUMERICAL SIMULATIONS

The proof of concept QPC set-up is formed with classically tractable number of planes and with simplicity to verify the main features of system design. Two different simulation experiments are achieved denoted by Sim_1 and Sim_2 , respectively. In Sim_1 , real numbers $b[n]$ for $n \in [0, N_p - 1]$ are chosen in a specific pattern to allow for highly accurate solution to SDA problem with significantly small error term. On the other hand, in Sim_2 , SDA problem is defined for less accurate solution with an optimization approach finding the term minimizing the error in a large interval. Two different QPC problems solved with the system set-up are shown in Table II. The presented numbers are rounded versions while digits of precision are improved in MATLAB used for simulations by utilizing variable precision arithmetic (vpa) to allow the contribution of path wave functions with significantly small amplitudes compared with the other paths. Main system parameters are shown in Table III where fundamental physical parameters are chosen based on electron beam based set-up verified for Gouy phase calculations in [31].

A. Simulation-1: Accurate SDA Solution and Effects of the Exotic Paths

The number of planes is set to two with $N = 3$ and $S_i = 2$ for $i \in [1, 2]$ to observe the main mechanism of QPC by explicitly analyzing wave functions on each plane and clearly observing effects of exotic paths. Total number of classical paths on image plane is $N_p = 25$ while the number of all paths including exotic ones, i.e., $N_{p,N}^E$, for varying N_E is shown in

TABLE II. QPC problems and simulation set-up parameters

ID	Property	Value
Sim_1	N, S_1, S_2	3, 2, 2
	\vec{X}_1^T, \vec{X}_2^T (nm)	$[-6031.9 \quad -2960.6 \quad 110.7 \quad 3181.9 \quad 6253.2], [-643.9 \quad -327.6 \quad -11.4 \quad 304.8 \quad 621.1]$
	\vec{d}^T (m ⁻²)	$[-11825366721.5 \quad -114848915118.2]$
	\vec{L}^T (m), $\vec{\beta}^T$ (nm)	$[1 \quad 400 \times 10^{-6} \quad 1], [196.5 \quad 63.2]$
Sim_2	N, S_1, S_2, S_3, S_4	5, 1, 1, 1, 1
	$\vec{X}_1^T, \vec{X}_2^T,$ \vec{X}_3^T, \vec{X}_4^T (nm)	$[-4315.4 \quad 382.0 \quad 3513.6], [-3610.0 \quad -570.0 \quad 950.0],$ $[-5887.7 \quad 506.0 \quad 2637.2], [-2312.9 \quad -230.0 \quad 3935.9]$
	\vec{d}^T (m ⁻²)	$[-36852879374.3 \quad -37760536805 \quad -25967723254.4 \quad -26078529374]$
	\vec{L}^T (m), $\vec{\beta}^T$ (nm)	$[1 \quad 476.2 \times 10^{-6} \quad 222.2 \times 10^{-6} \quad 175.4 \times 10^{-6} \quad 1], [191 \quad 190 \quad 230 \quad 230]$

TABLE III. Physical parameters

Symbol	Value	Symbol	Value
m (kg)	9.11×10^{-31}	\hbar (J \times s)	1.05×10^{-34}
v_z (m/s)	1.46×10^7	T_s (μ m)	1
σ_0 (nm)	500		

TABLE IV. Path counts on planes

	Sim_1		Sim_2			
	Plane-2	Sensor	Plane-2	Plane-3	Plane-4	Sensor
Classical	5	25	3	9	27	81
$N_E = 1$	25	625	9	81	729	6561
$N_E = 2$	105	11025	21	441	9261	194481
$N_E = 3$	425	180625	-	-	-	-

Table IV for both Sim_1 and Sim_2 . It is observed that as N_E increases, the number of exotic paths becomes significantly large complicating to find the final contribution on image plane. The simulated intensity converges as N_E increases and N_E is chosen as three and two for Sim_1 and Sim_2 , respectively, with reduced computational problems.

The fractional numbers forming the SDA problem are shown in Fig. 4(a). They are chosen with a special pattern to satisfy an accurate SDA solution at $\tilde{k} = 173$. Set-up parameters \mathbf{X}_{N-1}^s , \vec{d} , $\vec{\beta}$, \vec{L} , σ_0 and T_s are designed to provide desired set of real numbers. In Fig. 4(b), error terms $\bar{\epsilon}[M]$, $\epsilon_{max}[M]$ and $\epsilon_{min}[M]$ are shown for Sim_1 . The mean error term is smaller than 10^{-8} for $M = \tilde{k} = 173$, which is assumed to be SDA solution for the current problem with accuracy of eight digits.

In Fig. 4(c), normalized intensity $I_{norm}[k]$ is shown while $\tilde{I}[k]$ and $|H[k, 0]|^2$ are shown in Fig. 4(d) satisfying both the conditions in Theorem 1 such that $\tilde{I}[k] > \tilde{I}[0]$ and $\tilde{I}[k] < |H[k, 0]|^2$ for $k \leq \tilde{k}$. Therefore, the value of \tilde{k} is easily extracted by checking either periodicity or local maximum points of $\tilde{I}[k]$. Besides that, *IFFT* based method provides an accurate

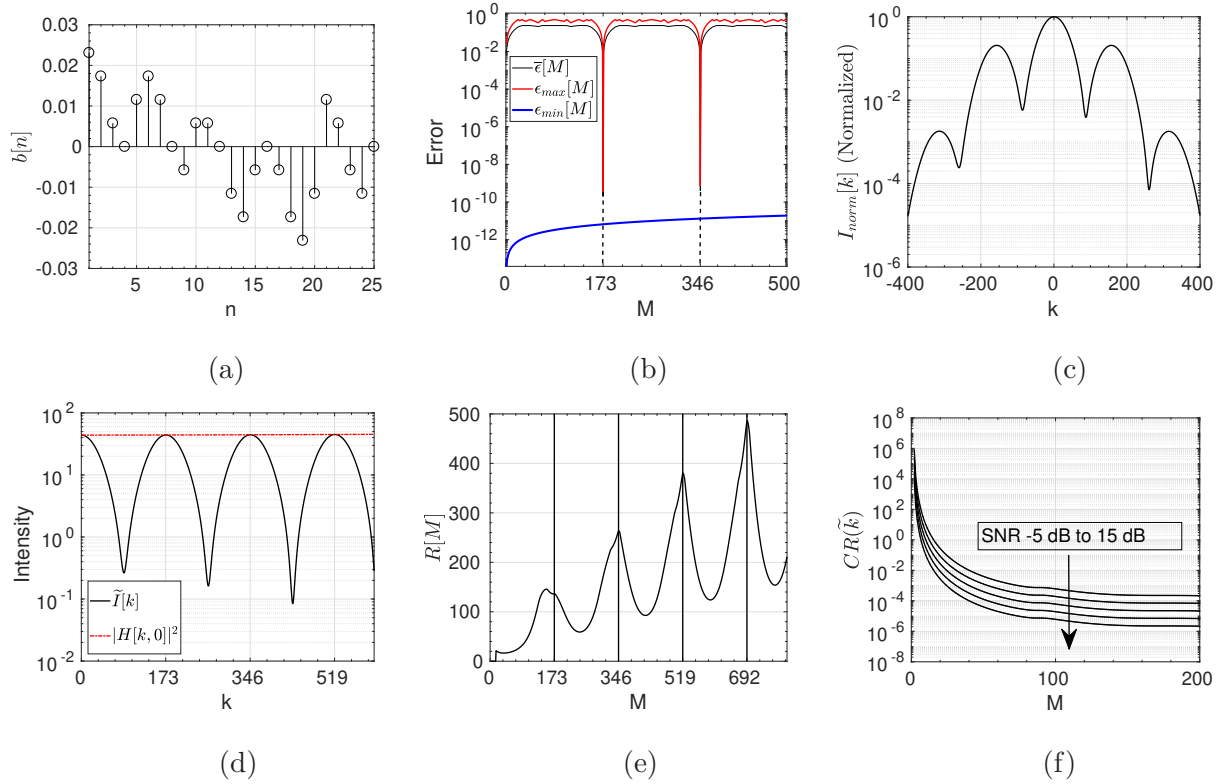


FIG. 4. (a) Distribution of real numbers $b[n]$ for $n \in [0, N_p - 1]$ defining SDA problem of Sim_1 , (b) error terms in SDA problem for varying M where the minimum error points are shown, (c) normalized intensity and (d) $\tilde{I}[k]$ on detector plane, (e) $R[M]$ for varying M showing high fluctuations around multiples of \tilde{k} , and (f) Cramer-Rao bound for estimating \tilde{k} for varying number of samples in $[0, M]$ and varying SNR in $[-5, 0, 5, 10, 15]$ dB.

estimation of \tilde{k} as shown in Fig. 4(e). Fluctuations are more visible as M increases at multiples of 173 while the maximum points of $R[M]$ show periodicity of 173. On the other hand, CRB is shown for varying SNR in Fig. 4(f) with a low bound for the number of samples larger than a few tens. Therefore, periodicity estimation methods for damped sinusoids can be applied successfully such as the ones in [39].

Effects of exotic paths are simulated in Figs. 5 and 6. In Fig. 6, intensity distribution on the planes of slits and image plane are shown. Five different peaks are clearly observed on the second plane while interfering pattern is shown on image plane and input wave function due to freely propagating Gaussian beam of electrons is shown on the first plane. Total normalized intensity distribution including exotic paths for varying N_E is shown in Fig. 5(a). The main structure of the distribution is preserved while effects for increasing N_E are

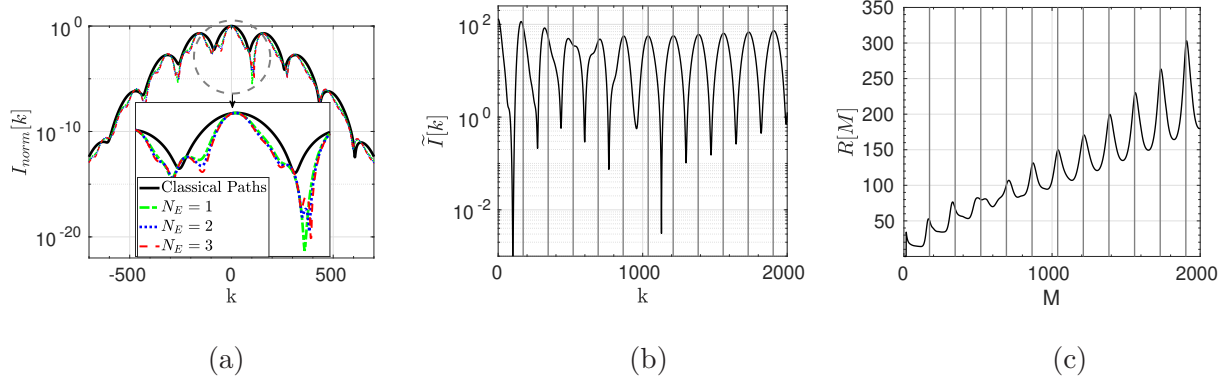


FIG. 5. (a) $I_{norm}[k]$ on image plane by including effects of exotic paths and for varying N_E where the middle part shows zoomed intensity distribution at the center, (b) $\tilde{I}[k]$ and (c) $R[M]$ for varying M for the case of $N_E = 3$ where the lines show multiples of $\tilde{k} = 173$.

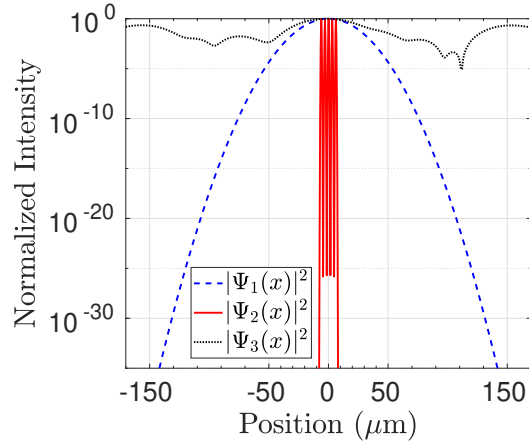


FIG. 6. Normalized intensity on the first, second and image planes including exotic paths.

attenuated as shown in Fig. 5(b) for the case of $N_E = 3$ where periodicity and the value of \tilde{k} are still reliably extracted. The same observation is preserved in $R[M]$ for varying M in Fig. 5(c). Periodicity extraction by utilizing smaller number of samples results in small errors in estimation of \tilde{k} while a converging estimation is observed for the specific problem in Sim_1 as the number of samples is increased. However, utilizing values of $\tilde{I}[k]$ for large k requires higher precision measurement instruments due to significant attenuation at distant sample locations and potentially longer time to collect particles. Special tuning and design of QPC set-up promise efficient solutions in future architectures based on the fundamental idea of QPC. Next, a larger SDA problem is solved by finding the optimum solution in a

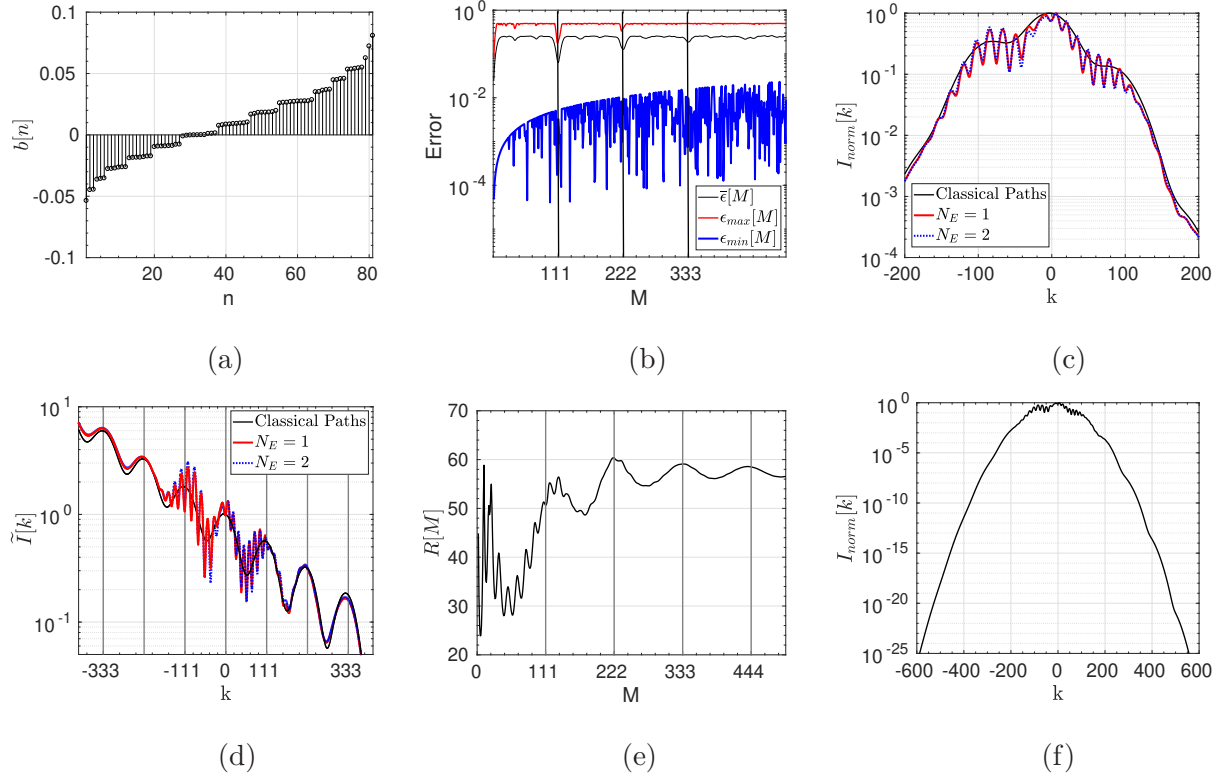


FIG. 7. (a) The set of 81 real numbers $b[n]$ defining the SDA problem of Sim_2 , (b) error terms in SDA problem for varying M where the minimum error point is shown at $M = 111$, (c) normalized intensity $I_{norm}[k]$ and (d) $\tilde{I}[k]$ on the detector plane for Sim_2 for both classical only paths and including the exotic contributions with $N_E = 1, 2$, (e) $R[M]$ for varying M for the case of $N_E = 2$, and (f) significant attenuation of $I_{norm}[k]$ at distant sample points.

given interval minimizing error terms.

B. Simulation-2: SDA Problem for Larger Inputs

The number of slit planes is increased to $N - 1 = 4$ and $S_i = 1$ for $i \in [1, 4]$ to realize a QPC solution for a more complicated problem by approximating SDA solution of 81 real numbers. The effect of exotic paths on image plane is calculated for $N_E = 2$ since the effects of the exotic paths gradually decrease and it is enough to calculate for $N_E = 1$ and $N_E = 2$ to observe the change in received intensity waveform.

The set of fractional real numbers is shown in Fig. 7(a) while error terms of SDA problem are shown in Fig. 7(b) with an approximate solution of $M = \tilde{k} = 111$ and with less accurate

solutions at multiples of \tilde{k} minimizing the error terms. QPC algorithm is utilized to find these optimum points by also including effects of exotic paths. Normalized intensity and $\tilde{I}[k]$ are shown in Figs. 7(c) and (d), respectively. Effects of exotic paths are more powerful at central part of image plane while still keeping the envelope with periodicity $\approx \tilde{k}$. Exotic path effects are smaller at non-central part of the sensor plane similar to the results of Sim_1 . IFFT based method finds multiples of $\tilde{k} = 111$ by utilizing samples in interval $[0, 500]$ as shown in Fig. 7(e) with small errors around \tilde{k} .

The model of the exact error in target periodicity is left as a future work. The important result is that QPC finds existence of periodicity and locates its position, for the specific example, with a high accuracy by using polynomial complexity calculations. Similarly, normalized intensity attenuates very fast requiring higher precision sampling or diversity combining methods to improve SNR at distant sampling locations. There is a trade-off between accuracy of periodicity extraction by utilizing distant points and SNR of the particles.

IX. DISCUSSION AND OPEN ISSUES

QPC system design requires further efforts to be utilized as an alternative computing architecture based on the solution of the challenges and open issues listed as follows. The provided system design is valid for other particles including photons for optical setups or molecules for molecular computing architectures for next generation nanoscale communication and computing systems. Open issues are the following:

1. Formal mathematical proof for the decision of SDA solution existence, i.e., \tilde{k} , depending on models of \vec{c} , \vec{d} , \mathbf{H} and A_j for $j \in [0, N - 1]$ with a metric for fluctuations compared with the other values in interval $1 \leq k \leq M$.
2. Defining the set of SDA problems formally whose solutions are achieved and not possible to achieve by a specific QPC set-up.
3. Extension of the set-up by combining Feynman's path integral formalism with operator formalism of entangled histories discussed in recent literature [19–22].
4. Providing the class of problems that QPC can exactly solve or provide an efficiently computed approximation, e.g., solutions of NP-hard or NP-intermediate problems [37].

5. Mapping from a target SDA problem to physical set-up parameters by utilizing complicated expressions of \vec{c} , \vec{d} , \mathbf{H} and A_j for $j \in [0, N - 1]$ described in Appendix A.
6. Designing the best classical frequency estimation method operating on samples of \tilde{I} by analyzing the state-of-the art polynomial solutions such as the ones reviewed in [39].
7. Experimental verification of the proposed system set-up and extension for other particles including photons and molecules by providing easier system design and utilization in molecular and nanoscale computing architectures.
8. Increasing number of planes results in lower intensity on image plane as a challenge to obtain enough counts of electrons in a reasonable time. The overall superposition intensity is utilized in QPC as an advantage compared with previous interference based QC attempts concentrating on a single path. On the other hand, increasing number and widths of slits, and the count of paths N_p improve the electron count on screen with less absorption on planes. QPC requires future efforts to clearly describe the trade-off among the size of the problem, efficiency of the solution and required energy of the particle source. Formal analysis of the trade-off is left as a future work.
9. As planes are getting closer, accuracy of assuming $t_{j,j+1}$ constant for all paths on j th plane decreases, and appears as an error term.
10. Gaussian slit approximation for particles should be verified experimentally or slits satisfying the Gaussian model should be realized. In approximation based methods, β_j for $j \in [1, N - 1]$ should be determined experimentally by tuning the value for a fixed slit width giving the smallest error in periodicity estimation. Photonic implementations with significantly thin planes, e.g., graphene or similar 2D materials, can be some candidates to form Gaussian slits for photonic QPC systems.

X. CONCLUSION

In this article, QPC architecture is presented as a novel QC system design by utilizing multi-plane and multi-slit simple interference set-up in combination with wave-particle duality, entangled path histories through slits and unique mathematical modeling based on

Feynman's path integral formalism. It provides a theoretical framework promising a candidate architecture for polynomial complexity solutions of HSPs and particular instances of SDA problems as important computational problems while requiring further efforts for theoretical modeling and experimental implementation. QPC system, as a simple design, combines wave-particle duality in an interference set-up by utilizing entangled path histories as qudit sources compared with previous interference architectures using only the wave nature and explicitly requiring exponential complexity of resources. In addition, theoretical modeling and simulation results extend previous interference formulations of exotic paths in single plane frameworks to multi-plane set-ups with multiple exotic paths showing their significant effects as a novel contribution. Open issues and challenges including theoretical and experimental aspects for realizing QPC prototypes are discussed in detail.

Appendix A

The first integration is obtained with $\Psi_0(x) = \exp(-x^2 / (2\sigma_0^2)) / \sqrt{\sigma_0} \sqrt{\pi}$ with free propagation until the first slit plane resulting in the following parameters:

$$A_0 = -\frac{m^2 \sigma_0^2}{2 \hbar^2 t_{0,1}^2 + 2 m^2 \sigma_0^4} \quad (\text{A1})$$

$$B_0 = \frac{\hbar m t_{0,1}}{2 \hbar^2 t_{0,1}^2 + 2 m^2 \sigma_0^4} \quad (\text{A2})$$

$$\chi_0 = \frac{1}{\pi^{1/4}} \sqrt{\frac{m \sigma_0}{m \sigma_0^2 + i \hbar t_{0,1}}} \quad (\text{A3})$$

while $C_0 = D_0 = 0$. The second LCT results in the following signal coefficients:

$$A_1 = \frac{\beta_1^2 m^2 (2 A_0 \beta_1^2 - 1)}{2 \zeta_1} \quad (\text{A4})$$

$$B_1 = \frac{2 B_0 \beta_1^4 m^2 + \hbar m t_{1,2} \varrho_1}{2 \zeta_1} \quad (\text{A5})$$

$$C_{n,1} = \zeta_{1,c} X_{1,s_n,1} \quad (\text{A6})$$

$$D_{n,1} = \zeta_{1,d} X_{1,s_n,1} \quad (\text{A7})$$

$$\chi_{n,1} = e^{p_{1,1} X_{1,s_n,1}^2} \sqrt{\xi_1} \quad (\text{A8})$$

where the following variables are defined:

$$p_{1,j} \equiv -(2 \hbar t_{j,j+1} (A_{j-1} + i B_{j-1}) + i m) / (2 i \varsigma_j)$$

$$\varsigma_j \equiv \beta_j^2 m + \hbar t_{j,j+1} (2 \beta_j^2 (B_{j-1} - i A_{j-1}) + i)$$

$$\xi_j \equiv \beta_j^2 m / \varsigma_j$$

$$\begin{aligned}
\varrho_j &\equiv 4\beta_j^4 (A_{j-1}^2 + B_{j-1}^2) - 4A_{j-1}\beta_j^2 + 1 \\
\zeta_j &\equiv 4B_{j-1}\beta_j^4 \hbar m t_{j,j+1} + \beta_j^4 m^2 + \hbar^2 t_{j,j+1}^2 \varrho_j \\
\zeta_{j,c} &\equiv (2B_{j-1}\hbar m t_{j,j+1}\beta_j^2 + \beta_j^2 m^2) / \zeta_j \\
\zeta_{j,d} &\equiv \hbar m t_{j,j+1} (2A_{j-1}\beta_j^2 - 1) / \zeta_j
\end{aligned}$$

Then, from the third LCT until the final plane, i.e., for $j \in [2, N-1]$, the following iterations are obtained:

$$A_j = \frac{\beta_j^2 m^2 (2A_{j-1}\beta_j^2 - 1)}{2\zeta_j} \quad (\text{A9})$$

$$B_j = \frac{2B_{j-1}\beta_j^4 m^2 + \hbar m t_{j,j+1} \varrho_j}{2\zeta_j} \quad (\text{A10})$$

$$C_{n,j} = \zeta_{j,c} X_{j,s_{n,j}} + p_{4,j} C_{n,j-1} + p_{5,j} D_{n,j-1} \quad (\text{A11})$$

$$D_{n,j} = \zeta_{j,d} X_{j,s_{n,j}} - p_{5,j} C_{n,j-1} + p_{4,j} D_{n,j-1} \quad (\text{A12})$$

$$\chi_{n,j} = \sqrt{\xi_j} e^{p_{1,j} X_{j,s_{n,j}}^2} e^{p_{2,j} (C_{n,j-1} + \imath D_{n,j-1})^2} e^{p_{3,j} (C_{n,j-1} + \imath D_{n,j-1}) X_{j,s_{n,j}}} \quad (\text{A13})$$

$$\chi_{T,j} = \chi_0 \prod_{k=1}^j \chi_{n,k} \quad (\text{A14})$$

where the following variables are defined:

$$p_{2,j} \equiv -\frac{\beta_j^2 \hbar t_{j,j+1}}{2\imath \zeta_j} \quad (\text{A15})$$

$$p_{3,j} \equiv -\frac{\hbar t_{j,j+1}}{\imath \zeta_j} \quad (\text{A16})$$

$$p_{4,j} \equiv \beta_j^2 \zeta_{j,c} \quad (\text{A17})$$

$$p_{5,j} \equiv \frac{-2\hbar t_{j,j+1}}{m} A_j \quad (\text{A18})$$

Then, if (A11) and (A12) are converted into a vectorial iterative relation, and including the path index n in the notations of C_j and D_j , the following is satisfied:

$$\begin{bmatrix} C_{n,j} \\ D_{n,j} \end{bmatrix} = \begin{bmatrix} \zeta_{j,c} \\ \zeta_{j,d} \end{bmatrix} X_{j,s_{n,j}} + \begin{bmatrix} p_{4,j} & p_{5,j} \\ -p_{5,j} & p_{4,j} \end{bmatrix} \begin{bmatrix} C_{n,j-1} \\ D_{n,j-1} \end{bmatrix} \quad (\text{A19})$$

Performing iterations result in $C_{n,N-1} = \vec{c}_{N-1}^T \vec{x}_{n,N-1}$ and $D_{n,N-1} = \vec{d}_{N-1}^T \vec{x}_{n,N-1}$ where j th element of the vector $\vec{x}_{n,N-1}$ of the length $N-1$ is defined as $X_{j,s_{n,j}}$, and the row vectors \vec{c}_j^T and \vec{d}_j^T are defined as follows:

$$\begin{bmatrix} \vec{c}_j^T \\ \vec{d}_j^T \end{bmatrix} \equiv \begin{bmatrix} \vec{v}_{0,j} & \vec{v}_{1,j} & \dots & \vec{v}_{j-1,j} \end{bmatrix} \quad (\text{A20})$$

and $\vec{v}_{k,j}$ for $k \in [0, j-1]$ to obtain $C_{n,j} = \vec{c}_j^T \vec{x}_{n,j}$ and $D_{n,j} = \vec{d}_j^T \vec{x}_{n,j}$ is given by the following:

$$\vec{v}_{k,j} = \left(\prod_{i=1}^{j-1-k} \begin{bmatrix} p_{4,j+1-i} & p_{5,j+1-i} \\ -p_{5,j+1-i} & p_{4,j+1-i} \end{bmatrix} \right) \begin{bmatrix} \zeta_{k+1,c} \\ \zeta_{k+1,d} \end{bmatrix} \quad (\text{A21})$$

where matrix multiplication symbol $\prod_{i=1}^k \mathbf{H}_i$ denotes $\mathbf{H}_1 \mathbf{H}_2 \dots \mathbf{H}_k$ for any matrix \mathbf{H}_i for $i \in [1, k]$. Putting the resulting expressions of $C_{n,N-1}$ and $D_{n,N-1}$ into (A13) and (A14), the following is obtained:

$$\begin{aligned} \chi_{T,N-1} &= \chi_0 \left(\prod_{j=1}^{N-1} \sqrt{\xi_j} \right) \left(\prod_{j=1}^{N-1} e^{p_{1,j} X_{j,s_{n,j}}^2} \right) \left(\prod_{j=2}^{N-1} e^{p_{2,j} (\vec{c}_{j-1}^T \vec{x}_{n,j-1} + \imath \vec{d}_{j-1}^T \vec{x}_{n,j-1})^2} \right) \\ &\quad \times \left(\prod_{j=2}^{N-1} e^{p_{3,j} (\vec{c}_{j-1}^T \vec{x}_{n,j-1} + \imath \vec{d}_{j-1}^T \vec{x}_{n,j-1}) X_{j,s_{n,j}}} \right) \end{aligned} \quad (\text{A22})$$

$$= \chi_0 \left(\prod_{j=1}^{N-1} \sqrt{\xi_j} \right) e^{\vec{p}_1^T \vec{g}_{n,1}} e^{\vec{p}_2^T \vec{g}_{n,2}} e^{\vec{p}_3^T \vec{g}_{n,3}} \quad (\text{A23})$$

where $\vec{p}_1^T \equiv [p_{1,1} \dots p_{1,N-1}]$, $\vec{p}_2^T \equiv [p_{2,2} \dots p_{2,N-1} 0]$, $\vec{p}_3^T \equiv [p_{3,2} \dots p_{3,N-1} 0]$, $\vec{g}_{n,1} \equiv [g_{n,1}(1) \dots g_{n,1}(N-1)]$, $\vec{g}_{n,2} \equiv [g_{n,2}(1) \dots g_{n,2}(N-2) 0]$, $\vec{g}_{n,3} \equiv [g_{n,3}(1) \dots g_{n,3}(N-2) 0]$, $g_{n,1}(j) \equiv X_{j,s_{n,j}}^2$ for $j \in [1, N-1]$, $g_{n,2}(j) \equiv (\vec{c}_j^T \vec{x}_{n,j} + \imath \vec{d}_j^T \vec{x}_{n,j})^2$ and $g_{n,3}(j) \equiv (\vec{c}_j^T \vec{x}_{n,j} + \imath \vec{d}_j^T \vec{x}_{n,j}) X_{j+1,s_{n,j+1}}$ for $j \in [1, N-2]$, and $g_{n,2}(N-1) \equiv g_{n,3}(N-1) = 0$. Then, by utilizing (A20), the following is obtained easily:

$$\begin{aligned} \chi_{T,N-1} &= \chi_0 \prod_{j=1}^{N-1} \sqrt{\xi_j} \exp \left\{ \vec{p}_1^T (\vec{x}_{n,N-1} \odot \vec{x}_{n,N-1}) \right\} \\ &\quad \times \exp \left\{ \vec{p}_2^T \left((\mathbf{G} \vec{x}_{n,N-1}) \odot (\mathbf{G} \vec{x}_{n,N-1}) \right) \right\} \exp \left\{ \vec{p}_3^T \left((\mathbf{G} \vec{x}_{n,N-1}) \odot (\mathbf{E}_1 \vec{x}_{n,N-1}) \right) \right\} \end{aligned} \quad (\text{A24})$$

where \odot denotes the point-wise product, and \mathbf{G} , \mathbf{E}_1 , \mathbf{E}_2 and \mathbf{V}_L are defined as follows:

$$\mathbf{V}_L \equiv \begin{bmatrix} \vec{v}_{0,1} & \mathbf{0}_2 & \dots & \mathbf{0}_2 \\ \vec{v}_{0,2} & \vec{v}_{1,2} & \dots & \mathbf{0}_2 \\ \vdots & \vdots & \vdots & \vdots \\ \vec{v}_{0,N-2} & \vec{v}_{1,N-2} & \dots & \vec{v}_{N-3,N-2} \end{bmatrix}; \quad \mathbf{G} \equiv \begin{bmatrix} \mathbf{E}_2 \mathbf{V}_L & \mathbf{0}_{N-2} \\ \mathbf{0}_{N-2}^T & 0 \end{bmatrix} \quad (\text{A25})$$

$$\mathbf{E}_1 \equiv \begin{bmatrix} \mathbf{0}_{N-2} & \mathbf{I}_{N-2} \\ 0 & \mathbf{0}_{N-2}^T \end{bmatrix}; \quad \mathbf{E}_2 \equiv \begin{bmatrix} 1 & \imath & 0 & 0 & \dots & 0 & 0 \\ 0 & 0 & 1 & \imath & \dots & 0 & 0 \\ \vdots & \vdots & \vdots & \vdots & \vdots & \vdots & \vdots \\ 0 & 0 & 0 & 0 & \dots & 1 & \imath \end{bmatrix} \quad (\text{A26})$$

while $\mathbf{0}_k$ is the column vector of zeros of length k , the sizes of \mathbf{E}_2 and \mathbf{V}_L are $(N-2) \times (2N-4)$ and $(2N-4) \times (N-2)$, respectively, and \mathbf{G} and \mathbf{E}_1 are $(N-1) \times (N-1)$.

Appendix B

The expression $\sum_{k=1}^3 \vec{\mathbf{p}}_k^T ((\mathbf{M}_{1,k} \vec{\mathbf{x}}_n) \odot (\mathbf{M}_{2,k} \vec{\mathbf{x}}_n))$ equals to the following:

$$\stackrel{1}{=} \sum_{k=1}^3 \text{Tr} \left\{ \text{diag}\{\vec{\mathbf{p}}_k\} \mathbf{M}_{1,k} \vec{\mathbf{x}}_n \vec{\mathbf{x}}_n^T \mathbf{M}_{2,k}^T \right\} \quad (\text{B1})$$

$$\stackrel{2}{=} \sum_{k=1}^3 \text{Tr} \left\{ \mathbf{M}_{2,k}^T \text{diag}\{\vec{\mathbf{p}}_k\} \mathbf{M}_{1,k} \vec{\mathbf{x}}_n \vec{\mathbf{x}}_n^T \right\} \quad (\text{B2})$$

$$\stackrel{3}{=} \text{Tr} \left\{ \left(\sum_{k=1}^3 \mathbf{M}_{2,k}^T \text{diag}\{\vec{\mathbf{p}}_k\} \mathbf{M}_{1,k} \right) \vec{\mathbf{x}}_n \vec{\mathbf{x}}_n^T \right\} \quad (\text{B3})$$

$$\stackrel{4}{=} \text{Tr} \left\{ \vec{\mathbf{x}}_n^T \left(\sum_{k=1}^3 \mathbf{M}_{2,k}^T \text{diag}\{\vec{\mathbf{p}}_k\} \mathbf{M}_{1,k} \right) \vec{\mathbf{x}}_n \right\} \quad (\text{B4})$$

where $\text{Tr}\{\cdot\}$ is the trace operator. The equality $\stackrel{1}{=}$ is obtained by transforming the inner and point-wise product combination into a trace operation. $\stackrel{2}{=}$ and $\stackrel{3}{=}$ are due to the permutation and the addition properties of the trace operation, respectively, while $\stackrel{4}{=}$ is due to the permutation property. Then, the quadratic form is obtained.

Appendix C

The intensity at $\tilde{k} - k$ for $k \in [1, \tilde{k}]$ is as follows:

$$\tilde{I}[\tilde{k} - k] \stackrel{1}{=} \left| \sum_{n=0}^{N_p-1} g_3[n] e^{g_1[n] (\tilde{k}-k)} e^{-\frac{j 2 \pi \tilde{G}_2[n] k}{k}} \right|^2 \quad (\text{C1})$$

$$\stackrel{2}{<} \left| \sum_{n=0}^{N_p-1} g_3[n] e^{g_1[n] (\tilde{k}-k)} \right|^2 \quad (\text{C2})$$

$$\stackrel{3}{<} \left| \sum_{n=0}^{N_p-1} g_3[n] e^{g_1[n] \tilde{k}} \right|^2 = \tilde{I}[\tilde{k}] \quad (\text{C3})$$

where $\stackrel{1}{=}$ is due to the definition in (12) and the first condition in Theorem 1, $\stackrel{2}{<}$ and $\stackrel{3}{<}$ are due to the second condition in Theorem 1.

Appendix D

The conditional probability for the sample at k_p is given by the following:

$$p(\tilde{I}_n[k_p]|\tilde{k}) = \frac{1}{\sqrt{2\pi\tilde{\sigma}_p^2}} e^{-\frac{(\tilde{I}_n[k_p] - \tilde{I}[k_p])^2}{2\tilde{\sigma}_p^2}} \quad (\text{D1})$$

where $\tilde{\sigma}_p \equiv \tilde{\sigma}[k_p]$. Then, denoting $\tilde{\mathbf{I}}_n = [\tilde{I}_n[k_0] \dots \tilde{I}_n[k_{M-1}]]^T$ and $\tilde{\mathbf{I}} = [\tilde{I}[k_0] \dots \tilde{I}[k_{M-1}]]^T$, the log likelihood function is given as follows:

$$\log(p(\tilde{\mathbf{I}}_n|\tilde{k})) = -\frac{M}{2} \log(2\pi) - \frac{1}{2} \sum_{p=0}^{M-1} \log(\tilde{\sigma}_p^2) - (\tilde{\mathbf{I}}_{n,\tilde{\sigma}} - \tilde{\mathbf{I}}_{\tilde{\sigma}})^T \cdot (\tilde{\mathbf{I}}_{n,\tilde{\sigma}} - \tilde{\mathbf{I}}_{\tilde{\sigma}}) \quad (\text{D2})$$

where $\tilde{I}_{n,\tilde{\sigma}}[k_p] = \tilde{I}_n[k_p] / (\tilde{\sigma}_p \sqrt{2})$ and $\tilde{I}_{\tilde{\sigma}}[k_p] = \tilde{I}[k_p] / (\tilde{\sigma}_p \sqrt{2})$. Fisher information matrix denoted by $I_F[\tilde{k}] \equiv E\{(\delta \log(p(\tilde{\mathbf{I}}_n|\tilde{k})) / \delta \tilde{k})^2\} = -E\{\delta^2 \log(p(\tilde{\mathbf{I}}_n|\tilde{k})) / \delta \tilde{k}^2\}$ for the zero mean random variable at each sample point is obtained after simple calculations as follows:

$$I_F[\tilde{k}] = \sum_{p=0}^{M-1} \frac{1}{\tilde{\sigma}_p^2} \left(\frac{\delta \tilde{I}[k_p]}{\delta \tilde{k}} \right)^2 \quad (\text{D3})$$

which depends on the square of the derivative of the intensity on the period \tilde{k} . Then, assuming an estimation method denoted by \hat{k} has a bias $b(\hat{k}) \equiv E\{\hat{k}\} - \tilde{k}$, the Cramer-Rao Bound, i.e., $CR(\tilde{k})$, for the variance of estimation is given by the following equality:

$$\text{Var}(\hat{k}) \geq CR(\tilde{k}) = \frac{(1 + \delta b(\hat{k}) / \delta \tilde{k})^2}{I_F[\tilde{k}]} \quad (\text{D4})$$

$$= \frac{(1 + \delta b(\hat{k}) / \delta \tilde{k})^2}{\sum_{p=0}^{M-1} \frac{e^{4 A_{N-1} (k_p T_s)^2}}{\sigma_p^2} \left(\frac{\delta \tilde{I}[k_p]}{\delta \tilde{k}} \right)^2} \quad (\text{D5})$$

Furthermore, assuming $\sigma_p^2 \leq \sigma_{max}^2$, the maximum of the minimum variance bound is given by the following:

$$CR(\tilde{k}) \leq \frac{\sigma_{max}^2 (1 + \delta b(\hat{k}) / \delta \tilde{k})^2}{\sum_{p=0}^{M-1} e^{4 A_{N-1} (k_p T_s)^2} (\delta \tilde{I}[k_p] / \delta \tilde{k})^2} \quad (\text{D6})$$

while with $\Delta G_2[n, l] \equiv \tilde{G}_2[l] - \tilde{G}_2[n]$, $\delta \tilde{I}[k_p] / \delta \tilde{k}$ is as follows:

$$\frac{\delta \tilde{I}[k_p]}{\delta \tilde{k}} = \sum_{n=0}^{N_p-1} \sum_{l=0}^{N_p-1} g_3[n] g_3^*[l] e^{(g_1[n] + g_1[l])k_p} e^{-\Delta G_2[n, l] \frac{i 2\pi k_p}{\tilde{k}}} \left(\Delta G_2[n, l] \frac{i 2\pi k_p}{\tilde{k}^2} \right) \quad (\text{D7})$$

Appendix E

The evolution of the wave function in n th path after the exotic travels of k slits as shown in Fig. 3 is as follows:

$$\Psi_{n,j,k}^E(x_{j,k}^E) = \int_{x_j} f_{n,k}^E(x_{j,k}^E, x_j) \Psi_{n,j,0}^E(x_{j,0}^E) dx_j \quad (\text{E1})$$

where $\Psi_{n,j,0}^E(x_{j,0}^E) \equiv G_{n,j}(x_j - X_{j,s_{n,j}}) \Psi_{n,j}(x_j)$, $f_{n,1}^E(x_{j,1}^E, x_j) \equiv K(x_{j,1}^E, t_{j,1}^E; x_j, t_j)$ and $f_{n,k}^E(x_{j,k}^E, x_j)$ for $k \geq 2$ is defined as follows:

$$\begin{aligned} f_{n,k}^E(x_{j,k}^E, x_j) &\equiv \int_{\vec{x}_{j;k}^E} d\vec{x}_{j;k}^E K(x_{j,1}^E, t_{j,1}^E; x_j, t_j) \\ &\times \prod_{p=2}^k K(x_{j,p}^E, t_{j,p}^E; x_{j,p-1}^E, t_{j,p-1}^E) G_{n,j}(x_{j,p-1}^E - X_{j,s_{n,j,p-1}}) \end{aligned} \quad (\text{E2})$$

while $k \in [1, N_E]$, $k = 0$ case corresponds to the wave-function evolution without any exotic path, i.e., $\Psi_{n,j,0}^E(x_{j,0}^E)$, $t_{j,k}^E \equiv \sum_{p=1}^k t_{p-1,p}^E(j) + t_j$ is the time after visiting k th slit on j th plane, t_j corresponds to the time at the beginning of the exotic movements, $\vec{x}_{j;k}^E \equiv [x_{j,1}^E \ x_{j,2}^E \ \dots \ x_{j,k-1}^E]$ and $x_{j,0}^E \equiv x_j$. Then, assuming that the n th path performs k consecutive visits to the slits on j th plane while the entrance slit is $X_{j,s_{n,j}}$ and the wave function at the position x_j is $\Psi_{n,j}(x_j)$, the wave function on the next plane, i.e., $\Psi_{n,j+1}(x_{j+1})$, becomes as follows:

$$\Psi_{n,j+1}(x_{j+1}) = \int K(x_{j+1}, t_{j,k}^E + t_{j,j+1}; x_{j,k}^E, t_{j,k}^E) G_{n,j}(x_{j,k}^E - X_{j,s_{n,j,k}}) \Psi_{n,j,k}^E(x_{j,k}^E) dx_{j,k}^E \quad (\text{E3})$$

-
- [1] R. P. Feynman, A. R. Hibbs, and D. F. Styer, *Quantum Mechanics and Path Integrals*, emended ed. (Dover Publications, Mineola, New York, USA, 2010).
 - [2] S. Lloyd, Physical Review A **61**, 010301 (1999).
 - [3] N. Bhattacharya, H. B. vanLindenvandenHeuvel, and R. J. C. Spreeuw, Phys. Rev. Lett. **88**, 137901 (2002).
 - [4] G. Puentes, C. La Mela, S. Ledesma, C. Iemmi, J. P. Paz, and M. Saraceno, Physical Review A **69**, 042319 (2004).
 - [5] V. Vedral, Foundations of Physics **40**, 1141 (2010).
 - [6] V. Černý, Physical Review A **48**, 116 (1993).

- [7] M. Oltean and O. Muntean, arXiv preprint [arXiv:1509.02673](https://arxiv.org/abs/1509.02673) (2015).
- [8] T. Haist and W. Osten, Optics Express **15**, 10473 (2007).
- [9] O. Muntean and M. Oltean, Journal of Optoelectronics and Advanced Materials **11**, 1728 (2009).
- [10] K. Wu, J. G. De Abajo, C. Soci, P. P. Shum, and N. I. Zheludev, Light: Science and Applications **3**, e147 (2014).
- [11] E. Cohen, S. Dolev, S. Frenkel, B. Kryzhanovsky, A. Palagushkin, M. Rosenblit, and V. Zakharov, JOSA A **30**, 1845 (2013).
- [12] D. Bigourd, B. Chatel, W. P. Schleich, and B. Girard, Phys. Rev. Lett. **100**, 030202 (2008).
- [13] J. F. Clauser and J. P. Dowling, Phys. Rev. A **53**, 4587 (1996).
- [14] J. Summhammer, Phys. Rev. A **56**, 4324 (1997).
- [15] A. Rangelov, Journal of Physics B: Atomic, Molecular and Optical Physics **42**, 021002 (2009).
- [16] V. Tamma, H. Zhang, X. He, A. Garuccio, W. P. Schleich, and Y. Shih, Phys. Rev. A **83**, 020304 (2011).
- [17] R. Jozsa and N. Linden, in *Proceedings of the Royal Society of London A: Mathematical, Physical and Engineering Sciences*, Vol. 459 (The Royal Society, 2003) pp. 2011–2032.
- [18] A. Ekert and R. Jozsa, Philosophical Transactions-Royal Society of London Series A: Mathematical Physical and Engineering Sciences , 1769 (1998).
- [19] J. Cotler and F. Wilczek, Physica Scripta **2016**, 014004 (2016).
- [20] J. Cotler, L. M. Duan, P. Y. Hou, F. Wilczek, D. Xu, Z. Q. Yin, and C. Zu, arXiv preprint [arXiv:1601.02943](https://arxiv.org/abs/1601.02943) (2016).
- [21] J. Cotler and F. Wilczek, arXiv preprint [arXiv:1503.06458](https://arxiv.org/abs/1503.06458) (2015).
- [22] M. Nowakowski, in *AIP Conference Proceedings*, Vol. 1841 (2017) p. 020007.
- [23] N. C. Jones, R. VanMeter, A. G. Fowler, P. L. McMahon, J. Kim, T. D. Ladd, and Y. Yamamoto, Phys. Rev. X **2**, 031007 (2012).
- [24] R. D. Somma, D. Nagaj, and M. Kieferova, Phys. Rev. Lett. **109**, 050501 (2012).
- [25] P. Bonderson, M. Freedman, and C. Nayak, Phys. Rev. Lett. **101**, 010501 (2008).
- [26] S. Aaronson and A. Arkhipov, in *Proc. of the Forty-third Annual ACM Symposium on Theory of Computing* (ACM, 2011) pp. 333–342.
- [27] H. Wang, Y. He, Y. H. Li, Z. E. Su, B. Li, H. L. Huang, X. Ding, M. C. Chen, C. Liu, J. Qin, *et al.*, Nature Photonics **11**, 361 (2017).

- [28] A. Stern and N. H. Lindner, *Science* **339**, 1179 (2013).
- [29] E. Gelenbe, *The Computer Journal* **55**, 848 (2012).
- [30] B. T. Gard, K. R. Motes, J. P. Olson, P. P. Rohde, and J. P. Dowling, *From atomic to mesoscale: The role of quantum coherence in systems of various complexities*. World Scientific Publishing Co. Pte. Ltd , 167 (2015).
- [31] I. G. daPaz, C. H. S. Vieira, R. Ducharme, L. A. Cabral, H. Alexander, and M. D. R. Sampaio, *Phys. Rev. A* **93**, 033621 (2016).
- [32] R. Sawant, J. Samuel, A. Sinha, S. Sinha, and U. Sinha, *Phys. Rev. Lett.* **113**, 120406 (2014).
- [33] A. Sinha, A. H. Vijay, and U. Sinha, *Scientific Reports* **5**, 1 (2015).
- [34] J. Q. Quach, *Phys. Rev. A* **95**, 042129 (2017).
- [35] J. C. Lagarias, in *IEEE 23rd Annual Symposium on Foundations of Computer Science* (1982) pp. 32–39.
- [36] H. Ozaktas, Z. Zalevsky, and M. A. Kutay, *The Fractional Fourier Transform with Applications in Optics and Signal Processing* (John Wiley and Sons, Chichester, UK, 2001).
- [37] M. A. Nielsen and I. L. Chuang, *Quantum Computation and Quantum Information* (Cambridge University Press, 2010).
- [38] Y. Meyer, *Beyond Quasicrystals: Quasicrystals, Diophantine Approximation and Algebraic Numbers* (Springer, 1995) pp. 3–16.
- [39] T. Zielinski and K. Duda, *Metrology and Measurement Systems* **18**, 505 (2011).